

THE LABOCA/ACT SURVEY OF CLUSTERS AT ALL REDSHIFTS: MULTI-WAVELENGTH ANALYSIS OF BACKGROUND SUBMILLIMETER GALAXIES.

PAULA AGUIRRE,¹ ROBERT R. LINDNER,^{2,3} ANDREW J. BAKER,² J. RICHARD BOND,⁴ ROLANDO DÜNNER,⁵ GASPAR GALAZ,⁵ PATRICIO GALLARDO,⁶ MATT HILTON,^{7,8} JOHN P. HUGHES,^{2,9} LEOPOLDO INFANTE,¹⁰ MARCOS LIMA,¹¹ KARL M. MENTEN,¹² JONATHAN SIEVERS,¹³ AXEL WEISS,¹² AND EDWARD J. WOLLACK¹⁴

¹*Escuela de Ingeniería, Pontificia Universidad Católica de Chile, Av. Vicuña Mackenna 4860, Macul, Santiago, Chile*

²*Department of Physics and Astronomy, Rutgers, The State University of New Jersey, 136 Frelinghuysen Road, Piscataway, NJ 08854-8019, USA*

³*Department of Astronomy, The University of Wisconsin-Madison, 475 N. Charter Street, Madison, WI 53706-1582, USA*

⁴*Canadian Institute for Theoretical Astrophysics, 60 St. George Street, University of Toronto, Toronto, ON, M5S 3H8, Canada*

⁵*Instituto de Astrofísica, Facultad de Física, Pontificia Universidad Católica de Chile, Av. Vicuña Mackenna 4860, Macul, Santiago, Chile*

⁶*Department of Physics, Cornell University, Ithaca, NY, 14853, USA*

⁷*Astrophysics and Cosmology Research Unit, School of Mathematics, Statistics & Computer Science, University of KwaZulu-Natal, Durban 4041, South Africa*

⁸*Centre for Astronomy and Particle Theory, School of Physics and Astronomy, University of Nottingham, Nottingham NG7 2RD, UK*

⁹*Center for Computational Astrophysics, Flatiron Institute, 162 Fifth Avenue, New York, NY 10010, USA*

¹⁰*Instituto de Astrofísica and Centro de Astroingeniería, Facultad de Física, Pontificia Universidad Católica de Chile, Av. Vicuña Mackenna 4860, Macul, Santiago, Chile*

¹¹*Departamento de Física Matemática, Instituto de Física, Universidade de São Paulo, São Paulo SP, Brazil*

¹²*Max-Planck-Institut für Radioastronomie, Auf dem Hügel 69, 53121, Bonn, Germany*

¹³*School of Chemistry and Physics, University of KwaZulu-Natal, Private Bag X54001, Durban 4000, South Africa*

¹⁴*NASA Goddard Space Flight Center, 8800 Greenbelt Road, Greenbelt, MD 20771, USA*

ABSTRACT

We present a multi-wavelength analysis of 48 submillimeter galaxies (SMGs) detected in the LABOCA/ACT Survey of Clusters at All Redshifts, LASCAR, which acquired new 870 μm and ATCA 2.1 GHz observations of ten galaxy clusters detected through their Sunyaev-Zel'dovich effect (SZE) signal by the Atacama Cosmology Telescope. Far-infrared observations were also conducted with the PACS (100/160 μm) and SPIRE (250/350/500 μm) instruments on *Herschel* for sample subsets of five and six clusters. LASCAR 870 μm maps were reduced using a multi-scale iterative pipeline that removes the SZE increment signal, yielding point-source sensitivities of $\sigma \sim 2 \text{ mJy beam}^{-1}$. We detect in total 49 sources at the 4σ level, and conduct a detailed multi-wavelength analysis considering our new radio and far-IR observations plus existing near-IR and optical data. One source is identified as a foreground galaxy, 28 SMGs are matched to single radio sources, 4 have double radio counterparts, and 16 are undetected at 2.1 GHz but tentatively associated in some cases to near-IR/optical sources. We estimate photometric redshifts for 34 sources with secure (25) and tentative (9) matches at different wavelengths, obtaining a median $z = 2.8^{+2.1}_{-1.7}$. Compared to previous results for single-dish surveys, our redshift distribution has a comparatively larger fraction of sources at $z > 3$ and the high-redshift tail is more extended. This is consistent with millimeter spectroscopic confirmation of a growing number of high- z SMGs and relevant for testing of cosmological models. Analytical lens modeling is applied to estimate magnification factors for 42 SMGs at cluster-centric radii $> 1.2'$; with the demagnified flux densities and source-plane areas, we obtain integral number counts that agree with previous submillimeter surveys.

Keywords: galaxies: clusters: general – cosmology: observations – submillimeter: galaxies – submillimeter: general

1. INTRODUCTION

Since the initial measurements of the cosmic infrared background (CIB; for a review see [Hauser & Dwek 2001](#)) revealed that the amount of energy radiated in the far-infrared (IR) and submillimeter spectral windows is comparable to that measured at ultraviolet (UV) and optical wavelengths, it has been widely recognized that one of the keys to a comprehensive understanding of the star formation history of the Universe is the study of the multi-wavelength properties of dusty star-forming galaxies (DSFGs) whose integrated radiation produce the CIB. These systems host intense star-forming activity obscured by large columns of dust, which re-emit the UV radiation of young hot stars at longer wavelengths, so that the peak of their rest-frame spectral energy distribution (SED) falls in the far-IR. In the local Universe, DSFGs are typically identified as luminous or ultra-luminous infrared galaxies (LIRGs/ULIRGs; [Sanders & Mirabel 1996](#)), whereas more distant DSFGs' emission can be redshifted into the submillimeter domain, allowing many to manifest as submillimeter galaxies (SMGs; [Blain et al. 2002](#); [Casey et al. 2014](#)). SMGs were first detected with the Submillimeter Common-User Bolometer Array (SCUBA; [Holland et al. 1999](#)) on the James Clerk Maxwell Telescope (JCMT) both in blank-field surveys (e.g., [Hughes et al. 1998](#); [Barger et al. 1999](#); [Scott et al. 2002](#); [Serjeant et al. 2003](#); [Webb et al. 2003](#); [Coppin et al. 2006](#)) and behind galaxy clusters (e.g., [Smail et al. 1997a](#); [Chapman et al. 2002](#); [Cowie et al. 2002](#); [Knudsen et al. 2008](#)). With the subsequent advent of comparable single-dish telescopes and larger format instruments covering the $870\ \mu\text{m}$ atmospheric window like the Large APEX Bolometer Camera (LABOCA; [Siringo et al. 2009](#)) on the 12-meter Atacama Pathfinder Experiment telescope (APEX; [Güsten et al. 2006](#)), and more recently SCUBA-2 ([Holland et al. 2013](#)), the number of known SMGs is now of the order of a few thousand (e.g., [Weiß et al. 2009](#); [Johansson et al. 2011](#); [Chen et al. 2013](#); [Hsu et al. 2016](#); [Geach et al. 2017](#)), and intensive observational efforts have been devoted to understanding their physical properties. In this quest, one of the main challenges has been the coarse ($15\text{--}20''$) resolution of single-dish observations, which hinders identification of counterparts at different wavelengths and can result in the blending of multiple, fainter SMGs into a single brighter object. However, persistence of the local radio-FIR correlation to higher redshifts (e.g., [Condon 1992](#)) allows determination of accurate SMG positions from deep radio imaging obtained with the Very Large Array (VLA) at 1.4 GHz and the Australia Telescope Compact Array (ATCA) at 2.1 GHz (e.g., [Ivison et al. 1998, 2000, 2002](#); [Smail et al. 2000](#); [Chapman et al. 2002](#)), thus

enabling identification of optical and near-IR counterparts, determination of photometric and spectroscopic redshifts (e.g., [Chapman et al. 2005](#)), modeling of SEDs, analysis of individual morphologies, and characterization of dust and stellar components (for full reviews of these results, see [Blain et al. 2002](#) and [Casey et al. 2014](#)). The general picture derived from such studies is that SMGs are massive, gas-rich galaxies with high IR luminosities ($L_{\text{IR}} \geq 10^{12} L_{\odot}$) and complex optical/near-IR morphologies, in which respects they resemble the local ULIRG population. However, SMGs have a median redshift $z \sim 2.5$ ([Chapman et al. 2005](#)) and significantly higher number density than ULIRGs. Complementary observations with centimeter and (sub)millimeter telescopes have been used as well to study the cool, molecular gas of SMGs (e.g., [Carilli & Walter 2013](#)), an effort that has been transformed in recent years thanks to the exceptional spatial resolution and sensitivity provided by the Jansky Very Large Array (VLA) and the Atacama Large Millimeter/submillimeter Array (ALMA). Moreover, high-resolution continuum imaging at $870\ \mu\text{m}$ with ALMA has made it possible to resolve the structure of the dust emission from SMGs and identify their counterparts in an unbiased way, revealing that a large fraction of bright single-dish detections actually “break up” into multiple, fainter ($S_{870} \lesssim 9\ \text{mJy}$) SMGs blended together at the coarse resolution of the maps in which they were detected ([Hodge et al. 2013](#); [Karim et al. 2013](#); [Simpson et al. 2015a,b](#)).

In addition to the classical SMG population selected at $\sim 850\ \mu\text{m}$, wide-field (sub)millimeter experiments like the Atacama Cosmology Telescope (ACT; [Swetz et al. 2011](#)) and the South Pole Telescope (SPT; [Carlstrom et al. 2011](#)) have detected significant numbers of strongly lensed, high- z DSFGs ([Vieira et al. 2010](#); [Marriage et al. 2011a](#); [Mocanu et al. 2013](#); [Marsden et al. 2014](#); [Su et al. 2017](#)), whose apparent luminosities and sizes are highly magnified by foreground galaxies or galaxy groups, thus enabling examination of their internal structures. This new subpopulation of DSFGs opens a new window for the study of high- z star-formation.

We note, however, that ACT and SPT surveys were primarily designed to measure cosmic microwave background (CMB) anisotropies and to detect the Sunyaev-Zel'dovich Effect (SZE; [Sunyaev & Zel'dovich 1972](#)) signals of galaxy clusters, which manifest as decrements relative to the CMB at observed frequencies $\nu < 220\ \text{GHz}$ and increments at $\nu > 220\ \text{GHz}$. ACT and SPT have produced sizable catalogs of new, massive clusters over a $z \sim 0.1 - 1.4$ redshift range (e.g., [Marriage et al. 2011b](#); [Reichardt et al. 2013](#); [Hasselfield et al. 2013](#); [Bleem et al. 2015](#)) that can be used to study the forma-

tion and evolution of the largest virialized structures in the universe, and to set constraints on cosmological parameters. Multiband follow-up of SZE-selected galaxy clusters is required to confirm the detections and investigate their internal physical properties; in the case of the ACT galaxy cluster sample, optical imaging and spectroscopy have been used in combination with X-ray data for assessment of sample purity, determination of redshifts, measurement of dynamical masses, and characterization of scaling relations (Menanteau et al. 2010a, 2012, 2013; Sifón et al. 2013, 2016). Near-IR photometry (Hilton et al. 2013) from the *Spitzer Space Telescope* (Werner et al. 2004) has been obtained as well to measure the stellar mass components of ACT clusters.

In Lindner et al. (2015) we introduced the LABOCA/ACT Survey of Clusters at All Redshifts, denoted LASCAR in honor of the homonymous active volcano in the north of Chile. This project comprises new observations at $870\ \mu\text{m}$ obtained with LABOCA ($19.6''$ resolution) and at $2.1\ \text{GHz}$ with ATCA ($\sim 5.0''$ resolution) of a set of ten massive clusters from the southern ACT sample. At submillimeter wavelengths, follow-up observation of SZE-selected clusters at higher spatial resolution than the $\sim 1'$ FWHM of the original detection maps has twofold appeal. First, at $870\ \mu\text{m}$ one can measure the SZE increment and constrain the shape of the thermal SZE spectrum; this information is used in turn to estimate the clusters' peculiar velocities and evaluate the scatter they introduce to scaling relations between mass and kinetic Sunyaev-Zel'dovich (kSZ) signal. Additionally, galaxy clusters serve as gravitational lenses for background point sources, thus allowing detection of magnified SMGs. Since point source emission is a significant contributor to the surface brightness in clusters at ACT frequencies, measurement of background SMG flux densities is essential to determine the degree of contamination of $148\ \text{GHz}$ decrements, and thus avoid biases in the SZE-mass relation and in the estimated number counts of clusters as function of mass and z (Sehgal et al. 2007, 2011). This contamination directly affects the cross-calibration and interpretation of SZE surveys, and therefore those surveys' ability to derive robust conclusions about cosmology.

Our initial paper (Lindner et al. 2015) focused on the measurement of the clusters' spatially resolved SZE increments, on the analysis of background and foreground contamination of this signal, and on estimation of the cluster's peculiar velocities. It was predicted in this work that the combined signals from $2.1\ \text{GHz}$ -selected radio sources and $870\ \mu\text{m}$ -selected SMGs contaminate the $148\ \text{GHz}$ SZE decrement signal by $\sim 5\%$, and the $345\ \text{GHz}$ SZE increment by $\sim 5\%$.

In this work, we present a multi-wavelength study of the submillimeter point source population detected in LASCAR, and use our original $870\ \mu\text{m}$ and $2.1\ \text{GHz}$ observations in combination with new far-IR imaging obtained with the Spectral and Photometric Receiver (SPIRE; Griffin et al. 2010) and the Photodetector Array Camera and Spectrometer (PACS; Poglitsch et al. 2010) on board the *Herschel Space Observatory*¹ (Pilbratt et al. 2010), plus existing optical and near-IR *Spitzer* data, to identify their plausible counterparts and investigate the general properties of background SMGs.

This paper is organized as follows: in Section 2 we give a detailed description of the clusters targeted in our submillimeter survey, and in Section 3 we present new submillimeter, radio, and far-IR observations of the LASCAR sample, and report on the data reduction techniques applied in each case. In Section 4 we describe additional datasets used in the analysis of SMGs, and Section 5 focuses on source extraction and photometry algorithms. In Section 6 we analyze sources (individually and collectively) detected in our data, including counterpart identification, estimation of redshifts and gravitational magnifications, and calculation of the redshift distribution and number counts for the SMG sample. Finally, Section 7 summarizes the conclusions derived from our survey. Throughout this work, we assume a flat ΛCDM cosmology with $H_0 = 70\ \text{km s}^{-1}\ \text{Mpc}^{-1}$, $\Omega_M = 0.27$, and $\Omega_\Lambda = 0.73$ (Komatsu et al. 2011).

2. CLUSTER SAMPLE

The ACT southern survey obtained $148\ \text{GHz}$ observations of a $455\ \text{deg}^2$ strip centered at $\text{Dec.} = -52.5^\circ$, which resulted in the identification of 23 cluster decrements (Marriage et al. 2011b), nine of them with signal to noise ratios $S/N > 6$, and 14 with S/N between 3 and 6. Optical follow-up (Menanteau et al. 2009, 2010b, see §4.2) confirmed that all decrements corresponded to rich galaxy clusters, ten of them newly discovered, and it was shown that the sample is 80% complete for clusters with masses larger than $6 \times 10^{14}\ M_\odot$ (Menanteau et al. 2010a).

From the set of 15 ACT clusters with highest S/N , we targeted 10 clusters that had not been previously mapped at submillimeter wavelengths, 9 of which were unknown before ACT or SPT. These clusters span a redshift range $z = 0.3 - 1.1$ and have dynamical masses $M_{500} = 5.2 - 11.3 \times 10^{14}\ M_\odot$ (Sifón et al. 2016), where

¹ *Herschel* is an ESA space observatory with science instruments provided by European-led Principal Investigator consortia and with important participation from NASA.

$M_{500} = 500(4\pi/3)\rho_c r_{500}^3$, and r_{500} is the radius enclosing a mass density equal to 500 times the critical density (ρ_c) of the Universe at the cluster’s redshift. Their physical properties are detailed in Table 1. The most studied cluster in this sample is ACT–CL J0102–4915, identified by Menanteau et al. (2012) as the most massive known cluster at high redshift ($z = 0.87$), and also known as “El Gordo”.

3. OBSERVATIONS AND DATA REDUCTION

3.1. LABOCA 870 μm

The LASCAR dataset consists of new 870 μm mapping of the ten galaxy clusters listed in Table 1 obtained with the LABOCA instrument at the APEX telescope. In the following subsections we give details on the observations and the reduction algorithm applied to these data.

3.1.1. LABOCA 870 μm observations

LABOCA observations of our cluster sample took place over three semesters (2010B, 2011A, 2011B) and were split among several proposals that amounted to a total of 140 hours of on-source time. All mapping was carried out in the standard spiral raster mode to concentrate on the central region ($< 8'$) in which the lensing magnification is expected to be highest. We aimed for a 1σ point source sensitivity of $\sim 1.5 \text{ mJy beam}^{-1}$, so as to allow 3σ detection of the $S(850\mu\text{m}) \geq 5 \text{ mJy}$ population. This is similar to the depths achieved by previous LABOCA and SCUBA surveys (Smail et al. 1997b; Knudsen et al. 2008; Weiß et al. 2009; Johansson et al. 2011).

Several types of calibration data were taken every $\sim 1 - 2$ hours to correct for instrumental and atmospheric effects. First, we obtained single spiral scans of planets and bright QSOs to measure and correct for deviations from the telescope pointing model, and also observed bright planets (Mars, Venus, Saturn, and Jupiter) regularly to verify and adjust the telescope focus. Second, we used regular sky dip observations to determine atmosphere opacity, which attenuates the astronomical signal detected in the LABOCA passband. Finally, planets and secondary calibrators with well known fluxes (Siringo et al. 2009) were observed in a raster-spiral mode to refine the canonical factor used to convert the raw data to physical units and improve the accuracy of the flux calibration. In general, the observing conditions encountered during our observations were good, with $\sim 80\%$ of our science scans obtained with wind speeds under 10 ms^{-1} and precipitable water vapor (PWV) under 1.0 mm .

3.1.2. LABOCA 870 μm data reduction

Our LABOCA observing campaign was designed to study simultaneously the 870 μm emission of SMGs and SZE clusters, and our data reduction process was therefore guided by the need to detect significant signals at different spatial scales. With this aim, we developed an iterative multi-scale algorithm that maximizes our sensitivity to low-level extended emission by applying a series of matched filters to search for signal at spatial extent of various scalers.. This pipeline is based on several standard data reduction routines implemented in the Bolometer Array Analysis Software (BoA²), and is described in full detail in Lindner et al. (2015).

Final flux density maps have a pixel scale of $3.6'' \text{ pix}^{-1}$, and the beam has a FWHM of $19.2''$. The iterative reduction applied to our LABOCA data resulted in an average root-mean-square (RMS) noise (σ) of $\sim 2 \text{ mJy beam}^{-1}$, as measured from the final beam-smoothed maps; individual σ values for each field are given in Table 2 and final signal to noise maps are presented in Figure 1. The effectiveness and reliability of our pipeline was tested on ESO archival LABOCA data for the “Bullet” cluster (1E0657-56; Markevitch et al. 2002), which was previously reduced by Johansson et al. (2010) using the CRUSH software.³ In their processing, they intentionally filter out the extended emission and therefore do not recover the SZE increment signal, but detect 17 point sources with $S/N > 4$. Comparison with results of our detection and photometry algorithm for this cluster is presented in Section 5.

For the LASCAR sample, we detect point sources in all fields, and strong SZE increment signals ($S/N > 3.5$) in six clusters (see Table 2). Lindner et al. (2015) present a thorough multi-wavelength analysis of the SZE increments, and in the following sections we focus on the extraction, photometry, and analysis of unresolved sources.

3.2. ATCA 2.1 GHz observations

We have conducted deep, high-resolution continuum mapping at 2.1 GHz of all ten clusters with ATCA. These data are crucial to facilitate identification of counterparts for the submillimeter emission detected with LABOCA. The observations were carried out in January 2011, December 2011, and April 2012 using the 16 cm-band receiver with the CFB 1M-0.5k correlator mode, which gives a bandwidth of 2 GHz with 2048×1 -

² <http://www.apex-telescope.org/bolometer/laboca/boa>

³ <http://www.submm.caltech.edu/sharc/crush/>

Figure 1. LABOCA 870 μm signal-to-noise maps for the sample of ten clusters targeted by LASCAR. Circles indicate the locations of all detected point sources, as listed in Table 5.

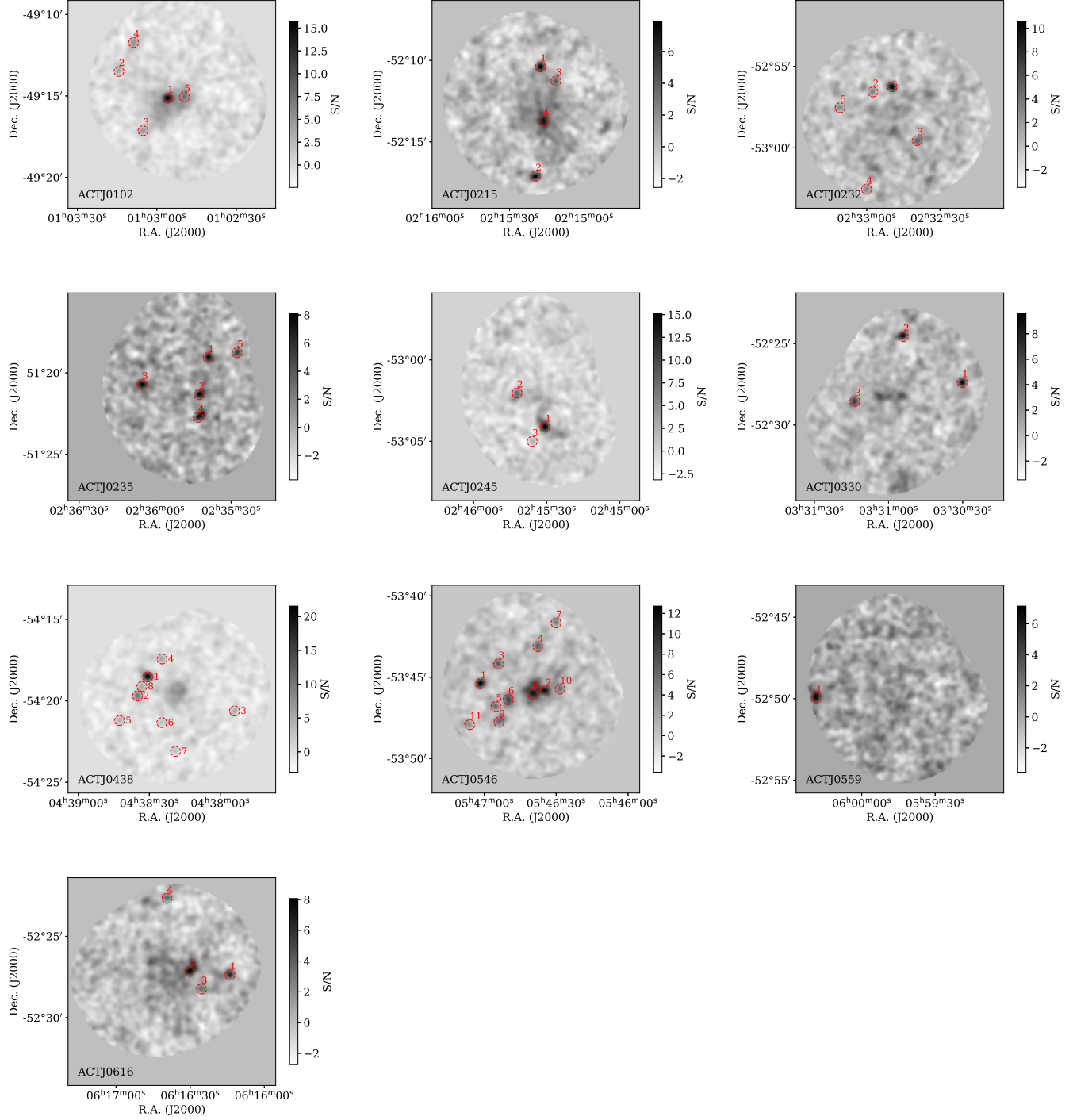


Table 1. Galaxy clusters mapped with LABOCA at 870 μm .

Target	R.A. (J2000)	Dec. (J2000)	z	Dynamical mass ($10^{14} M_{\odot}$)	ACT S/N
ACT-CL J0102-4915	01:02:52.5	-49:14:58.0	0.87008 \pm 0.00010	11.3 \pm 2.9	9.0
ACT-CL J0215-5212	02:15:12.3	-52:12:25.3	0.48009 \pm 0.00012	7.6 \pm 2.3	4.9
ACT-CL J0232-5257	02:32:46.2	-52:57:50.0	0.55595 \pm 0.00009	5.2 \pm 1.4	4.7
ACT-CL J0235-5121	02:35:45.3	-51:21:05.2	0.27768 \pm 0.00006	8.0 \pm 2.0	6.2
ACT-CL J0245-5302	02:45:35.8	-53:02:16.8	0.30280 \pm 0.00001	...	9.1
ACT-CL J0330-5227	03:30:56.8	-52:28:13.7	0.44173 \pm 0.00009	11.6 \pm 2.7	6.1
ACT-CL J0438-5419	04:38:17.7	-54:19:20.7	0.42141 \pm 0.00011	12.9 \pm 3.2	8.0
ACT-CL J0546-5345	05:46:37.7	-53:45:31.1	1.06628 \pm 0.00020	5.5 \pm 2.3	6.5
ACT-CL J0559-5249	05:59:43.2	-52:49:27.1	0.60910 \pm 0.00026	8.3 \pm 3.0	5.1
ACT-CL J0616-5227	06:16:34.2	-52:27:13.3	0.68380 \pm 0.00044	9.5 \pm 4.5	5.9

NOTE—Column 1 indicates the cluster name; Columns 2 to 5 correspond to the coordinates, redshift, and mass estimate for each cluster. Column 6 indicates the signal to noise ratio of the ACT 148 GHz detections (from [Marriage et al. 2011b](#)). Coordinates for all LASCAR clusters correspond to the positions of the brightest cluster galaxies (BCGs) identified by [Menanteau et al. \(2010a\)](#). For all clusters the redshifts and masses are based on the spectroscopic measurements of [Sifón et al. \(2016\)](#), except for ACT-CL J0245-5302, for which we use the spectroscopic measurement of [Ruel et al. \(2014\)](#).

Table 2. LABOCA 870 μm observations.

Target	Period	P.I.	Observation dates	On-source time (hr)	σ (mJy beam $^{-1}$)	SZE S/N
ACT-CL J0102-4915	2011B ^a	A. Baker	2011 Aug 20-28	11.3	2.4	9.7
ACT-CL J0215-5212	2011B	L. Infante	2011 Oct 1-4	17.6	2.4	8.2
ACT-CL J0232-5257	2010B	A. Baker	2010 Aug 6-10	17.0	2.0	4.3
ACT-CL J0235-5121	2011A	A. Baker	2011 Jul 14-26	12.2	1.7	2.2
ACT-CL J0245-5302	2011B	A. Weiß	2011 Oct 21-26	11.6	2.1	2.9
ACT-CL J0330-5227	2010B	A. Baker	2010 Oct 16-21	8.1	1.9	2.1
ACT-CL J0438-5419	2010B	A. Baker	2010 Aug 23-24 2010 Oct 13-21	28.3	1.6	8.8
ACT-CL J0546-5345	2010B	L. Infante	2010 Aug 26-27 2010 Oct 26-29	16.3	1.6	8.2
ACT-CL J0559-5249	2011A	L. Infante	2011 Jul 26-30	13.3	2.8	1.8
ACT-CL J0616-5227	2011B	A. Baker	2011 Sep 7-12 2011 Nov 4-5	14.8	2.1	7.7

^a Director's Discretionary Time (DDT) proposal.

MHz channels.⁴ All clusters have been observed with the 6A antenna configuration; ACTJ0102-4915 was also observed in the 1.5B configuration. The integration time per cluster is indicated in Table 3. For flux and band-pass calibration we used PKS 1934-638 (Reynolds 1994); for phase calibration, we selected an appropriate bright, nearby and compact source for each cluster.

For ATCA data reduction we used the MIRIAD software package (Sault et al. 1995); details are given in Lindner et al. (2015). Final maps have RMS sensitivities from 6.9 to 12.0 $\mu\text{Jy beam}^{-1}$, and synthesized beams have major axes $\sim 4 - 6''$ (see Table 3). We used the Common Astronomy Software Applications (CASA; McMullin et al. 2007) to extract point sources above a 4σ threshold and measured their flux densities by fitting 2-D Gaussian profiles with the beam shapes and position angles given in Table 3. The combined number counts over all fields follow a power law $dN/dS \propto S^{-\delta}$, with index $\delta = 1.7$ (Lindner et al. 2015), where S is the flux density.

3.3. *Herschel* observations

In our efforts to characterize the far-IR through submillimeter SEDs of point sources detected by LABOCA and constrain at the same time the clusters' SZE spectra, we obtained new *Herschel Space Observatory* observations for the subset of six clusters from our full LASCAR sample listed in Table 4. These targets were selected based on their high masses and strong SZE decrement signals, and all six of them were mapped at 250, 350, and 500 μm with SPIRE; five of the six were also observed at 100 and 160 μm using PACS.

3.3.1. *Herschel*/PACS observations and data reduction

New PACS observations of five LASCAR clusters followed the observational strategy of the *Herschel* Lens Survey (HLS, Egami et al. 2010), using the scan-map mode with medium speed and 13 scan legs of $4'$ each with a $20''$ cross-scan step that result in $8' \times 8'$ maps. To control optimally for systematics, each cluster was observed twice by orthogonal scan maps with orientation angles of 45° and 315° , with 18 repetitions each. The total on-source time for each cluster was 1.6 hours.

All observations were reduced interactively using version 11.1.0 of the *Herschel* Interactive Processing Environment (HIPE, Ott 2010) using PACS calibration version 41 and scripts supplied with HIPE. The standard processing of raw data includes pixel flagging, flux

density conversion, coordinate registration, high-pass filtering to remove background structure, and spatial deglitching. Individual maps were mosaiced to remove $1/f$ noise from scanning. Final maps have an image scale of $1'' \text{ pix}^{-1}$ in both bands, RMS noise of ~ 3.8 (3.3) mJy beam^{-1} , and angular resolution of $6''$ ($13''$) at 100 (160) μm . For detection and photometry of point sources, we applied the same extraction algorithm used for construction of the 870 μm catalog, which is described in detail in Section 5.

3.3.2. *Herschel*/SPIRE observations and data reduction

SPIRE observations of the six clusters in Table 4 used the Large Map mode, and in all cases except for ACT-CL J0330-5227 consisted of four repetitions of $8' \times 8'$ maps at four dithered positions, which account for a total of 2224 s on-source time. For ACT-CL J0330-5227, we performed only four repetitions of a $6' \times 6'$ map at a single position, with a total on-source time of 492 s. Data reduction and map-making follow standard procedures implemented within HIPE, and resulted in angular resolutions of 17.6, 23.9, and $35.0''$, pixel scales of 6, 10 and $14'' \text{ pix}^{-1}$, and RMS map sensitivities of 7.4, 7.2, and 7.2 mJy beam^{-1} at 250, 350, and 500 μm , respectively (excluding ACT-CL J0330-5227; see Table 4). To remove the SZE signal and extract point sources, we used the 250 μm map to derive a model for the confused SMG background at 350 and 500 μm , as detailed in Section 3.7 of Lindner et al. (2015). The final confusion noise-free maps have mean RMS sensitivities $\sim 3 \text{ mJy beam}^{-1}$, and we apply a 4.5σ threshold for detection of point sources.

4. COMPLEMENTARY DATA

As part of the ACT collaboration's efforts to achieve complete multi-wavelength follow-up of SZE-detected clusters, targets in the LASCAR sample had been previously observed in the near-IR with the *Spitzer Space Telescope* and in the optical with ground based telescopes. In the following subsections we summarize relevant information regarding these observations; details of their reduction and analysis have been published in previous work.

4.1. *Spitzer*/IRAC data

All clusters in the LASCAR sample were imaged with the InfraRed Array Camera (IRAC; Fazio et al. 2004) on *Spitzer*, at wavelengths of 3.6 and 4.5 μm , through a proposal that targeted 14 confirmed ACT clusters with

⁴ <http://www.narrabri.atnf.csiro.au/observing/CABB.html>

Table 3. Properties of 2.1 GHz ATCA Radio Maps for LASCAR Clusters.

Target	Integration time (hr)	σ ($\mu\text{Jy beam}^{-1}$)	Beam	P.A. ($^{\circ}$)
ACT-CL J0102-4915	12.1	7.5	$6.1'' \times 3.1''$	-1.9
ACT-CL J0215-5212	8.6	11.0	$4.7'' \times 2.9''$	-21.0
ACT-CL J0232-5257	19.8	8.1	$4.8'' \times 3.1''$	6.0
ACT-CL J0235-5121	8.5	10.9	$5.3'' \times 2.7''$	-10.0
ACT-CL J0245-5302	10.3	10.5	$4.4'' \times 3.0''$	4.3
ACT-CL J0330-5227	8.8	11.7	$5.1'' \times 2.7''$	17.7
ACT-CL J0438-5419	8.1	11.9	$5.3'' \times 2.8''$	-19.6
ACT-CL J0546-5345	21.0	6.9	$4.7'' \times 3.2''$	-3.1
ACT-CL J0559-5249	8.9	9.6	$5.4'' \times 2.9''$	-13.3
ACT-CL J0616-5227	7.8	12.0	$5.0'' \times 3.0''$	26.6

Table 4. *Herschel* PACS and SPIRE observations of LASCAR clusters.

Target	Observation ID	Observation date	σ_{100}	σ_{160}	σ_{250}	σ_{350}	σ_{500}
ACT-CL J0102-4915	1342256977	2012-12-11	3.79	3.03	7.4	7.2	7.4
ACT-CL J0235-5121	1342262209	2013-01-27	3.83	3.26	7.4	7.2	7.4
ACT-CL J0245-5302	1342262466	2013-01-28	3.83	3.39	7.4	7.2	7.4
ACT-CL J0330-5227	1342259282	2013-01-17	9.4	8.2	8.4
ACT-CL J0438-5419	1342259282	2013-01-17	3.71	3.42	7.4	7.2	7.4
ACT-CL J0546-5345	1342261752	2013-01-21	3.75	3.25	7.4	7.2	7.4

NOTE—For each target we give dataset specifications, and the RMS noise (σ_{λ}) of final maps for observation wavelengths $\lambda = 100, 160, 250, 350$, and $500 \mu\text{m}$, in mJy beam^{-1} .

$0.27 < z < 1.07$ (PI: Menanteau, PID: 70149). Observations took place in August 2010 - July 2011; they were designed to provide coverage out to the clusters' virial radii, using 2×2 grids of IRAC pointings centered on the cluster positions. Details on the observations, data reduction, and photometry algorithms have been published in Menanteau et al. (2012) and Hilton et al. (2013). The resulting catalog is 80% complete for point sources at $m_{\text{AB}} \sim 22.6$ mag in both channels.

4.2. Optical data

The original catalog of ACT SZE-detected cluster candidates was followed up in the optical to confirm their nature and determine the purity of the ACT sample. The optical campaign started in semester 2009B and consisted of 7 nights of observations at 4m class telescopes in Chile (3.6 m NTT at La Silla and 4.1 m SOAR Telescope at Cerro Pachón). All targets were observed using either the Gunn or SDSS *griz* filter sets, and the final images have pixel scales of $0.24'' \text{ pix}^{-1}$ ($0.15'' \text{ pix}^{-1}$) for NTT (SOAR). The full details of observa-

tions, data reduction, and analysis are given in Menanteau et al. (2010a). The final catalogs are estimated to be 80% complete down to magnitudes $i = 23.5$ (NTT) and $i = 24.3$ (SOAR), and the multi-band photometry was used to estimate photometric redshifts, although the associated errors are relatively large due to the limited number of filters. In this work, we use *griz* photometric catalogs to investigate the existence of optical counterparts for our SMGs at least down to the quoted limiting magnitudes.

In addition to *griz* imaging, Sifón et al. (2013) carried out deep multi-object spectroscopic observations for a sample of 16 massive ACT clusters and obtained intermediate-resolution ($R \sim 700 - 800$) spectra and redshifts for ~ 60 member galaxies per cluster. These data were used to measure dynamical masses (M_{200}) and radii (r_{200}) for their clusters, which include all LASCAR targets except ACT-CL J0245-5302, a previously known cluster (Abell S0295). As will be described in Section 6.3, these results are of great utility for modeling

the lensing properties of our clusters and estimating the magnifications of the detected background sources. The full tables containing the magnitudes and spectroscopic redshifts of the galaxies targeted by Sifón et al. (2013) are available online, and are also used in this work to check if any of our submillimeter sources coincide with known cluster members.

5. SOURCE EXTRACTION AND PHOTOMETRY

The signal in each of our LABOCA and *Herschel* maps is a combination of point source emission from DSFGs located in front of, in, and behind each galaxy cluster, possibly magnified by its gravitational potential in the latter case, and the cluster’s SZE increment signal. In Lindner et al. (2015), we report the extraction and measurement of the integrated SZE flux densities from LABOCA and SPIRE maps, and here we focus on the detection and photometry of submillimeter point sources and measurement of their multi-wavelength properties.

To optimize extraction and photometry of point sources in LABOCA and *Herschel* data, we use a hybrid algorithm that combines median filtering with the matched-filter technique of Serjeant et al. (2003) that is typically applied to maps with non-uniform noise. First, we preprocess the final pipeline-produced flux density image by subtracting the median filtered version with a kernel size equal to three times the beam’s FWHM, so as to optimize detection of point sources above even bright diffuse background signals, like those we expect in the clusters’ central region. Next, we generate a minimal- χ^2 signal-to-noise map according to the formula

$$S/N = \frac{(SW) \otimes P}{\sqrt{W \otimes P^2}} \quad (1)$$

where S is the pre-processed image signal, W is the pixel weight map generated in the data reduction pipeline, P is the image Gaussian point-spread function and \otimes denotes a convolution (Serjeant et al. 2003). We use this optimal map to locate the positions of unresolved sources with $S/N > 4$, and then measure their flux densities in the original image *without* median filtering.⁵ At each point-source position, we fit a 2-D Gaussian with a fixed center and a FWHM equal to that of the map’s beam, and allow for a varying, non-negative peak amplitude plus a constant offset to account for the background signal.

With the described algorithm we have detected a total of 49 new submillimeter point sources over ten cluster

fields, with 870 μm flux densities ranging from 6.6 to 33.9 mJy. All LABOCA source positions, flux densities, and S/N ratios are listed in Table 5; sources are circled in the LABOCA S/N maps presented in Figure 1. To test our data reduction and source extraction pipeline, we have applied the same methodology to archival data for the extensively studied “Bullet” cluster, which has been observed with LABOCA (Johansson et al. 2010), PACS, and SPIRE (Egami et al. 2010), among many other instruments. We have generated an optimal-S/N 870 μm point source catalog in the exact manner as for the LASCAR clusters, and compare our results with those of Johansson et al. (2010). We detect in total seven point sources, five of which are also contained in their catalog and have flux density measurements that are in good agreement, with a mean relative difference of 16%. The two remaining sources that are not selected by Johansson et al. (2010) are relatively fainter ($S_{870} \sim 9.5$ mJy) and located within the 148 GHz decrements measured by ACT (Marriage et al. 2011b), so the discrepancy may be explained by the aggressive filtering applied by those authors to remove the extended SZE signal. Inspection of archival PACS data (Egami et al. 2010) reveals that one of them also has a 100/160 μm counterpart.

On the other hand, Johansson et al. (2010) report in total 13 point sources within the central 10’ of which we do not recover one 8.2 mJy source that is identified with a foreground galaxy, and seven fainter sources with $S_{870} \leq 6.2$ mJy. From their multiwavelength analysis, four of these sources lack IRAC or 24 μm counterparts, and we verify that they are also undetected in PACS imaging. Hence, there is no further confirmation of their authenticity. The three remaining sources do have 24 μm or PACS counterpart candidates and would be extracted with our hybrid algorithm using a lower threshold of 3σ , which increases however the number of spurious detections. Overall, we find that our data reduction and source extraction methods are in good agreement with the results of Johansson et al. (2010) in terms of detection and photometry for sources with flux densities above ~ 6.5 mJy, but in both cases there is a tradeoff between detection of faint SMGs and possible contamination of spurious sources below this limit. Hence, we favor the more conservative results obtained with our pipeline with a 4σ threshold. Additionally, the careful treatment of the extended 870 μm emission and removal of the cluster’s SZE increment implemented in our pipeline improves extraction of point sources that overlap with the SZE signal.

To estimate the completeness of our detections, we follow a procedure similar to that used by Knudsen et al.

⁵ Median filtering is beneficial for suppression of diffuse background noise, but may remove flux from sources in a complex morphology-dependent way.

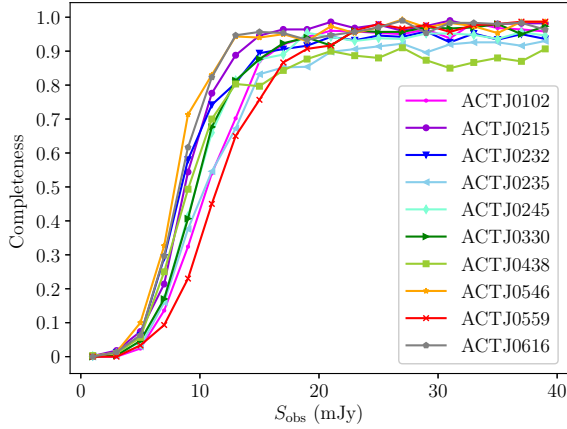


Figure 2. Completeness of LABOCA point source detections for each cluster, estimated from simulations, and represented in terms of the fraction of detected over total sources versus observed flux density S_{obs} .

(2008), Weiß et al. (2009), and Johansson et al. (2011): we add point sources of varying flux densities at ran-

dom positions to the flux density maps shown in Figure 1, run the detection pipeline with the same settings as for the actual cluster maps, and compare the resulting detections with the input source catalog to determine the fraction of recovered sources. The artificial point sources are modeled by a Gaussian profile with a FWHM equal to the LABOCA beam ($19.2''$), peak amplitudes from 0.5 to 40 mJy in steps of 0.5 mJy, and random (x, y) positions following a uniform distribution. For each field, at each flux density step, we simulate 100 sets of 10 sources each, apply our hybrid extractor to produce a S/N map and detect point sources at the 4σ level, and calculate the mean detection rate. In comparing the simulated and detected catalogs, we consider as matching detections those within one beam width of the input positions. The results of our completeness analysis for each cluster are shown in Figure 2; on average we reach a 90% detection rate at a flux density ~ 18 mJy, and as expected, the completeness at a given flux limit is higher in those maps with lower average noise levels.

Table 5. LABOCA $870\mu\text{m}$ point sources detected in the fields of the clusters in our sample.

Source ID	R.A. (J2000)	Dec. (J2000)	$S(870\mu\text{m})$ (mJy)	$\Delta S(870\mu\text{m})$ (mJy)	S/N	θ (arcmin)	z_{phot}	μ
ACTJ0102-1	01:02:55.9	-49:15:09.1	33.9	1.44	13.8	0.6	4.5 ± 0.6	5.6^c
ACTJ0102-2	01:03:14.2	-49:13:30.3	20.2	1.60	6.6	3.8	4.5 ± 0.8^a	1.0^c
ACTJ0102-3	01:03:05.1	-49:17:08.9	13.0	1.28	6.0	3.0	4.2 ± 0.5	1.9^c
ACTJ0102-4	01:03:08.7	-49:11:44.1	14.6	1.56	5.9	4.2	2.0 ± 0.6	1.0^c
ACTJ0102-5	01:02:49.6	-49:15:04.4	18.9	1.66	5.1	0.5	1.1 ± 0.7	1.6^c
ACTJ0215-1	02:15:17.6	-52:10:24.5	18.5	1.19	9.0	2.2	...	1.1 ± 0.1
ACTJ0215-2	02:15:19.6	-52:17:07.0	15.4	1.09	9.2	4.8	...	1.0 ± 0.1
ACTJ0215-3	02:15:11.3	-52:11:16.8	10.2	1.11	4.4	1.2
ACTJ0215-4	02:15:16.4	-52:13:44.1	7.5	1.04	4.1	1.5	...	1.3 ± 0.1
ACTJ0232-1	02:32:49.6	-52:56:15.7	16.9	1.0	10.3	1.7	4.5 ± 0.2	1.1 ± 0.1
ACTJ0232-2	02:32:57.4	-52:56:34.9	10.4	1.0	5.0	2.1	2.8 ± 0.6	1.1 ± 0.1
ACTJ0232-3	02:32:39.3	-52:59:34.2	8.2	0.9	5.1	2.0	...	1.1 ± 0.1
ACTJ0232-4	02:33:00.1	-53:02:33.2	8.9	1.1	4.7	5.2	1.5 ± 0.7	1.0 ± 0.0
ACTJ0232-5	02:33:10.8	-52:57:33.1	7.1	1.2	4.1	3.7	1.7 ± 0.4	1.0 ± 0.1
ACTJ0235-1	02:35:39.1	-51:19:04.6	15.3	1.4	6.0	2.2	...	1.2 ± 0.1
ACTJ0235-2	02:35:42.7	-51:21:21.0	16.2	1.5	6.2	0.5	2.9 ± 0.7^a	...
ACTJ0235-3	02:36:05.1	-51:20:43.6	11.3	1.2	5.6	3.1	0.018^b	...
ACTJ0235-4	02:35:43.0	-51:22:44.7	12.1	1.1	5.7	1.7	4.0 ± 0.7^a	1.3 ± 0.1
ACTJ0235-5	02:35:27.7	-51:18:46.2	16.9	1.6	5.7	3.6	3.7 ± 0.6^a	1.1 ± 0.1
ACTJ0245-1	02:45:30.6	-53:04:08.7	22.4	1.3	11.1	2.0	4.0 ± 0.6^a	1.2 ± 0.1
ACTJ0245-2	02:45:42.1	-53:02:02.4	11.0	1.2	4.8	1.0	2.1 ± 0.6	...
ACTJ0245-3	02:45:35.9	-53:05:01.5	9.6	1.2	3.9	2.7	3.8 ± 0.5	1.1 ± 0.1
ACTJ0330-1	03:30:30.3	-52:27:24.1	21.9	1.2	11.4	4.1	3.0 ± 0.5^a	1.1 ± 0.1

Table 5 continued

Table 5 (*continued*)

Source ID	R.A.	Dec.	$S(870\ \mu\text{m})$	$\Delta S(870\ \mu\text{m})$	S/N	θ	z_{phot}	μ
	(J2000)	(J2000)	(mJy)	(mJy)		(arcmin)		
ACTJ0330-2	03:30:54.0	-52:24:35.0	20.9	1.3	9.0	3.7	3.2 ± 1.0	1.1 ± 0.1
ACTJ0330-3	03:31:13.6	-52:28:33.5	13.1	1.2	6.5	2.6	1.7 ± 0.7	1.1 ± 0.1
ACTJ0438-1	04:38:30.6	-54:18:32.4	33.3	1.0	21.4	2.0	3.4 ± 0.7^a	1.3 ± 0.1
ACTJ0438-2	04:38:34.9	-54:19:42.0	16.8	1.0	10.3	2.5	3.2 ± 0.6^a	1.2 ± 0.1
ACTJ0438-3	04:37:54.0	-54:20:37.8	8.1	0.8	6.6	3.7	...	1.1 ± 0.1
ACTJ0438-4	04:38:24.6	-54:17:26.6	12.6	1.0	6.1	2.1	...	1.3 ± 0.1
ACTJ0438-5	04:38:42.5	-54:21:13.3	9.1	1.1	5.2	4.1	3.5 ± 0.8	1.1 ± 0.0
ACTJ0438-6	04:38:24.7	-54:21:21.0	7.6	0.9	4.4	2.2	...	1.2 ± 0.1
ACTJ0438-7	04:38:18.9	-54:23:07.2	6.6	0.9	4.1	3.8	...	1.1 ± 0.0
ACTJ0438-8	04:38:33.1	-54:19:07.9	7.4	1.0	4.0	2.3	...	1.2 ± 0.1
ACTJ0546-1	05:47:01.4	-53:45:24.5	21.4	1.0	14.3	3.5	4.9 ± 0.9	1.0 ± 0.0
ACTJ0546-2	05:46:34.5	-53:45:51.9	12.9	1.0	7.5	0.6	1.9 ± 0.7	...
ACTJ0546-3	05:46:53.9	-53:44:12.3	12.2	1.0	7.5	2.7	2.2 ± 0.8	1.0 ± 0.0
ACTJ0546-4	05:46:37.6	-53:43:07.9	12.7	0.9	7.4	2.4	4.5 ± 0.9	1.0 ± 0.1
ACTJ0546-5	05:46:55.0	-53:46:48.7	10.9	0.9	6.2	2.9	2.7 ± 1.0	1.0 ± 0.1
ACTJ0546-6	05:46:49.9	-53:46:22.9	7.2	0.9	6.1	2.0	...	1.0 ± 0.1
ACTJ0546-7	05:46:30.1	-53:41:40.6	13.9	1.4	5.5	4.0	3.2 ± 0.1	1.0 ± 0.0
ACTJ0546-8	05:46:39.9	-53:46:02.9	8.3	1.0	4.9	0.6	2.3 ± 0.5^a	...
ACTJ0546-9	05:46:53.8	-53:47:46.5	7.0	0.9	4.8	3.3	2.1 ± 0.4	1.0 ± 0.0
ACTJ0546-10	05:46:28.4	-53:45:44.4	7.1	0.9	4.3	1.4	3.2 ± 1.0	1.1 ± 0.2
ACTJ0546-11	05:47:05.9	-53:47:55.5	7.6	1.0	4.2	4.8	1.9 ± 0.7	1.0 ± 0.0
ACTJ0559-1	06:00:18.5	-52:49:57.8	18.4	1.9	5.4	5.3	2.9 ± 1.0	1.0 ± 0.0
ACTJ0616-1	06:16:13.9	-52:27:23.6	12.4	1.1	6.6	3.1	1.1 ± 0.4	1.0 ± 0.1
ACTJ0616-2	06:16:30.3	-52:27:10.6	13.7	1.1	6.4	0.6
ACTJ0616-3	06:16:25.5	-52:28:15.1	7.7	1.0	4.3	1.7	...	1.2 ± 0.1
ACTJ0616-4	06:16:39.3	-52:22:41.0	12.5	1.3	4.4	4.6	3.9 ± 0.7	1.0 ± 0.0

NOTE—

The first column indicates the source identifier, formed by the name of the cluster in whose field it was detected, plus a correlative ID number that ranks sources in a field according to their S/N ratio. The equatorial coordinates indicate the location of the source's centroid in the $870\ \mu\text{m}$ S/N map; the integrated flux density $S(870\ \mu\text{m})$ is measured from the reduced, non-smoothed flux density map, and the signal to noise ratio S/N is obtained from the Gaussian-filtered map. The last columns indicate the angular distance to the cluster's center (θ), the photometric redshift estimated from SED modeling when possible, and the magnification factor (μ) estimated from the models described in Section 6.3.

^a Tentative counterpart identifications.

^b Redshift of foreground galaxy ESO 198-G021, see Appendix A. No magnification is considered for this source.

^c From Zitrin et al. (2013) magnification maps.

6. ANALYSIS OF $870\ \mu\text{m}$ POINT SOURCES

In this section we study the multi-wavelength properties of the set of SMGs detected by LASCAR at $870\ \mu\text{m}$. First we identify their counterparts in the radio, far-IR, near-IR, and optical regimes, model their SEDs and estimate photometric redshifts when possible, estimate their magnification due to lensing by the clusters, and analyze the resulting redshift distribution and number counts.

6.1. Counterpart identification

To identify the multi-wavelength counterparts of LASCAR SMGs, we searched the radio, PACS, SPIRE,

IRAC and optical catalogs described above and identified as preliminary counterpart candidates all sources located within a circle of radius equal to half the LABOCA beam's FWHM ($19.2''$) centered on a position in Table 5. We then applied the following criteria:

- Among the available data, the best resource for accurate SMG localization is the deep 2.1 GHz imaging, so we start by identifying a matching radio source when possible, and then use the radio centroid as a reference for counterpart identification at shorter wavelengths. To evaluate the reliability of the association of the SMG with a radio source of flux density $S_{2.1}$ located within

the LABOCA beam, we calculate the corrected Poisson probability of a chance detection within a beam’s area around the submillimeter centroid (P_C) as:

$$P_C = 1 - \exp \left\{ -P^* \left[1 + \ln \left(\frac{P}{P^*} \right) \right] \right\} \quad (2)$$

where P^* is the raw Poisson probability of finding a source brighter than $S_{2.1}$ inside a search radius $r = 9.6''$, and P is the raw probability of finding a source brighter than the critical radio detection flux density in the same region (Downes et al. 1986). Both are calculated as $1 - \exp(-\pi n r^2)$, where n is the integral number density of radio sources above a given flux. For the radio source number counts, we scale the 2.1 GHz flux densities to 1.4 GHz assuming a radio spectral index $\alpha = -0.75$ (Ibar et al. 2010), and adopt the 1.4 GHz differential number counts function obtained by Bondi et al. (2008) for the VLA-COSMOS survey, which yielded a catalog of ~ 3600 radio sources over a 2 deg^2 region, down to a 1σ sensitivity limit of about $11 \mu\text{Jy}$. This catalog has a resolution of $1.5''$, but only $\sim 7\%$ of all sources form pairs with angular separation smaller than the resolution of our radio imaging. The traditional approach is to require $P_C < 0.05$ for a reliable radio-submillimeter association. In our analysis, we consider a single radio counterpart candidate with $P_C < 0.05$ as a secure identification, and if there is more than one radio source within the LABOCA beam meeting this requirement, we consider them to define a multiple-component source. We then use the radio positions to look for PACS, IRAC, and optical matches within a search radius of $2''$, which is the mean circularized radius of the synthesized beam for our ATCA imaging. Finally, if there are no reliable radio detections within the LABOCA beam, we set an upper limit for the 2.1 GHz flux density and proceed to the analysis of FIR candidate counterparts.

- In the absence of a significant radio detection, we move on to inspection of PACS images, which have been shown to have SMG detection rates of $\sim 40 - 50\%$ at $160 \mu\text{m}$, for a 3σ detection limit $\sim 5.7 \text{ mJy}$ and sample median redshifts $\langle z \rangle \sim 2$ (Dannerbauer et al. 2010; Magnelli et al. 2010). Again, we apply the $P_C < 0.05$ criterion for a reliable association and calculate the probability of chance association between the LABOCA and PACS source based on the PACS differential number counts obtained by Berta et al. (2010) for the GOODS-N and COSMOS fields at 100 and $160 \mu\text{m}$. The PACS coordinates are used as the reference to search for matching sources at shorter wavelengths. However, given that 100 and $160 \mu\text{m}$ maps have beam FWHMs of

7.2 and $12''$, respectively, in some cases two or more IRAC/optical matches may be blended together by the far-IR beam, hindering precise counterpart identification.

- SPIRE $250/350/500 \mu\text{m}$ maps have spatial resolutions that are comparable to or poorer than that of our LABOCA imaging. Therefore, SPIRE detections within the LABOCA beam are considered counterparts to the $870 \mu\text{m}$ emission and add data points to the SED modeling, but do not provide improved source positioning or aid in the identification of counterparts in other bands.
- For clusters with no *Herschel*/PACS observations, we are only able to pinpoint the near-IR/optical counterpart if there is a radio detection. Otherwise, we are only able to select a candidate counterpart among IRAC sources that fall within the LABOCA beam based on their $S_{4.5}/S_{3.6}$ color, which we expect to be comparable to the median 1.27 ± 0.24 observed for an SMG sample by Hainline et al. (2009). These are recorded as “tentative” identifications.

In Appendix A, we give a brief description of the counterpart identification process for each of the 49 submillimeter sources in our catalog, and in Figures 8 to 17 we show multi-wavelength postage stamps for the SMGs in each cluster. All results are summarized in Tables 7 and 18, where we respectively list the flux densities and coordinates of counterparts identified in radio, SPIRE, PACS, IRAC, and optical data.

In total, we find that out of 49 submillimeter sources, one coincides with a foreground galaxy (ACTJ0235–3). Of the remaining 48 SMGs, 4 have no identifiable counterparts in the available bands, 26 have single radio counterparts, 4 have double radio counterparts, and 14 are not detected in radio mapping, but have tentative counterpart identifications in the far or near-IR. The last column of Table 7 indicates in which category each source falls.

6.2. SED Modeling and Photometric Redshifts

Michałowski et al. (2010) used a set of 76 SMGs ($S_{850} \gtrsim 3 \text{ mJy}$) with spectroscopic redshifts $z = 0.080 - 3.623$ and dust temperatures $T_D = 11.4 - 113.3 \text{ K}$ from the sample of Chapman et al. (2005) to model the entire UV-to-radio spectral SEDs of a statistically significant sample in a self-consistent way. Their modeling was based on a library of 35,000 models from Iglesias-Páramo et al. (2007), which were developed in GRASIL (Silva et al. 1998), cover a broad range of galaxy properties from quiescent to starburst, and include a set of

templates based on nearby ULIRGs (Silva et al. 1998) and gamma-ray burst host galaxies (Michałowski et al. 2008). Michałowski et al. (2010) matched these templates to all available UV to radio photometry simultaneously for each source, obtaining a library of best-fitting SMG SEDs that exhibits a wide range of stellar population properties. Smolčić et al. (2012) tested these templates on eight SMGs with spectroscopic redshifts and found that the implied photometric redshifts were in better agreement than those obtained with other models drawn from the Bruzual & Charlot (2003) library or provided by the public code Hyper-z (Bolzonella et al. 2000).

We used this library and our radio, submillimeter, far-IR, and near-IR measurements to estimate photometric redshifts for all LASCAR SMGs with secure radio, PACS, and/or SPIRE counterparts, and also for LASCAR sources with no radio counterparts but with tentative near-IR matches, as indicated in Table 7. For each SMG, we redshifted all templates from $z = 0$ to $z = 8$ in even steps of $\Delta z = 0.05$, scaled the spectra to match the observed $870 \mu\text{m}$ flux density, and calculated the resulting χ^2 statistic. We find that with the limited number of data points currently available, is it not possible to discriminate with confidence between different SEDs that give comparably good fits at different redshifts, and determination of a “best-fitting” redshift based solely on χ^2 minimization can be misleading. Therefore, our preferred approach is to find the best-fitting redshift for each model in the Michałowski et al. (2010) library, select those templates for which the resulting χ^2 is among the 10% lowest values, and average the corresponding photometric redshifts to determine a mean optimal redshift, with an associated dispersion. Although this procedure results in photometric estimates with rather large errors, of order $\Delta z \sim 1$, it gives a realistic representation of the uncertainties in the determination of SMG redshifts based on a limited number of observations. If we relax the 10% limit to include a larger set of best-fitting redshifts, the mean results are similar but dispersion increases; for example, if the 25% lowest values are selected instead, photometric redshifts vary on average by $\sim 9\%$, but the associated errors are $\sim 12\%$ larger.

In total, we model the SEDs of 34 sources, 25 of which correspond to secure counterpart identifications and 9 of which are only tentative estimates. In Appendix A, Figure 18, we show our SED fits. For each source we plot observed flux densities, flux density upper limits for non-detections when appropriate, and the range of best SED fits that we consider in our calculations of the mean photometric redshift. In Figure 3 we plot the resulting $N(z)$ distribution for sources with robust and

tentative counterparts, together with previous literature results for comparison.

For the sample with robust and tentative counterpart identifications, the median redshifts are $z = 2.8^{+2.1}_{-1.7}$ and $z = 3.4^{+1.1}_{-1.1}$, respectively. These results are in reasonable agreement with those from Chapman et al. (2005) (median $z = 2.2 \pm 0.1$ for a radio pre-selected sample); from the LABOCA Extended Chandra Deep Field South (ECDFS) submillimeter survey (LESS; Wardlow et al. 2011; median $z = 2.2 \pm 0.1$); and also with the more recent ALMA surveys of Danielson et al. (2017) (median $z = 2.4 \pm 0.1$) and Brisbin et al. (2017) (median $z = 2.48 \pm 0.05$). In our photometric redshift distribution there is a comparatively larger fraction of sources at $z > 3$, and the high-redshift tail extends further out than that of the LESS distribution including one SMG with $z_{\text{phot}} \sim 4.9$. The existence of this tail is consistent with millimeter spectroscopic confirmation of a growing number of SMGs at $z \gtrsim 4$ (e.g., Capak et al. 2008; Weiß et al. 2013; Smolčić et al. 2012, 2015; Strandet et al. 2016), and with the spectroscopic and photometric redshift distributions obtained by Danielson et al. (2017) and Brisbin et al. (2017) for samples of SMGs observed at the spatial resolution of ALMA. Su et al. (2017) also estimate photometric redshifts for nine strongly lensed DSFGs selected by ACT at 218 GHz (1.4 mm) and obtain a higher median redshift $z = 4.1^{+1.1}_{-1.0}$, which is expected since the highest-redshift sources remain bright at this lower frequency due to the negative K -correction.

Our photometric redshift estimates support the existence of a $z \gtrsim 4$ SMG population, but it is unclear whether these sources’ number counts are consistent with the predictions of cosmological models. For example, semianalytic models that assume a top-heavy IMF and star formation driven by merger-triggered starbursts (Baugh et al. 2005) predict a redshift distribution centered at $z \sim 2$, with very few sources at much higher redshifts. As a reference, the expected redshift distribution from Baugh et al. (2005) predicts that only $\sim 5\%$ of SMGs with $S_{850} = 8 \text{ mJy}$ ($S_{870} \sim 7.5 \text{ mJy}$) lie at $z > 4$, so for our subset of 25 SMGs with robust counterpart identifications we would expect only 1–2 objects in this redshift range, in contrast to the ~ 5 that we estimate (Table 5). Additional data are critical to confirm the existence and abundance of very high- z SMGs in our sample and confirm or refute our preliminary results; in particular, high-resolution submillimeter imaging is key to confirm counterpart identification for SMGs that are undetected at radio wavelengths.

6.3. Gravitational magnification

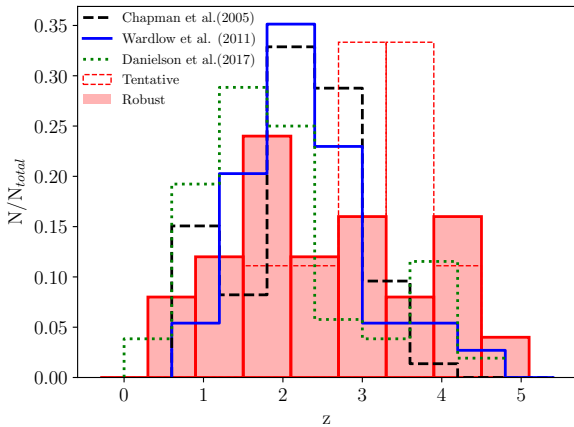


Figure 3. Redshift distribution for SMGs detected in LASCAR. Results of this work are plotted in red. The filled histogram shows the redshift distribution for 25 sources with robust radio/near-IR counterparts, for which the median value is $z = 2.8 \pm 0.7$. The dashed histogram corresponds to the redshift distribution of sources with tentative counterparts, with a median $z = 3.4^{+1.1}_{-1.1}$. For comparison we include the normalized results from Chapman et al. (2005) (black, dashed), Wardlow et al. (2011) (blue, solid) and Danielson et al. (2017) (green, dotted).

The detection of SMGs in LASCAR may be facilitated by the foreground galaxy clusters acting as gravitational lenses, but the resulting flux magnifications also affect the analysis of the intrinsic counts distribution and enhance the scatter in the contamination of the SZ signal. The amplification of each source depends exclusively on the mass distribution and geometrical configuration of the intervening structures relative to the source position, with no need for additional assumptions regarding their dynamical state (Limousin et al. 2007). The effect is strongest close to a cluster’s core, where the mass surface density is high enough to produce strong lensing features like arcs and multiple images, which can be used to reconstruct the gravitational potential and then calculate the resulting magnification as a function of position. However, such analysis requires very deep and high-resolution optical imaging combined with extensive spectroscopy to detect lensed images and measure the redshifts of a lens and of a collection of background objects. Datasets typically used to build successful models include multi-band *HST* imaging and ground-based spectroscopy using 8-10 m telescopes (e.g. Jullo et al. 2007; Limousin et al. 2007, and references therein). Among LASCAR clusters, such data are partially available only for ACT-CL J0102–4915, for which Zitrin et al. (2013) present a strong-lensing analysis. For the remaining clusters, we are unable to construct de-

tailed lensing models at present, but we can use an analytic approach to approximate the magnifications affecting our detected SMGs, and estimate how strongly lensing affects our number counts and other results. From inspection of our optical and near-IR imaging, we find no evidence of superposition with individual lens galaxies that might boost local magnification, so in our calculations we account only for the effects of the clusters’ gravitational potentials.

To estimate magnifications for the LASCAR clusters, we follow the rationale and equations presented in Lima et al. (2010a,b): we adopt a density profile to model the cluster’s dark matter halo, derive the analytical form of lensing observables like the shear and convergence, and finally use the basic lensing equations to calculate the magnification at each projected cluster-centric radius. We assume that the cluster dark matter halo mass density is well represented by a Navarro-Frenk-White (NFW; Navarro et al. 1997) spherical profile with a characteristic virial mass M_{200} , corresponding to the mass within a sphere of a radius r_{200} whose mean interior is density $200\rho_{\text{crit}}$, for ρ_{crit} the critical density for a flat universe. Our calculations are based on the results of Sifón et al. (2016), who used deep optical spectroscopy to determine M_{200} and r_{200} for all clusters in our sample except ACT-CL J0245–5302, which was known before the ACT detection (e.g., Abell et al. 1989; Voges et al. 1999; Edge et al. 1994; Wu & Fang 1997) and therefore not included in their observations. To evaluate M_{200} for ACT-CL J0245–5302, we apply the scaling relation in Sifón et al. (2016):

$$\sigma_{200} = A_{1D} \left[\frac{hE(z)M_{200}}{10^{15}M_{\odot}} \right]^{\alpha} \quad (3)$$

where σ_{200} is the line-of-sight velocity dispersion in a spherical cluster of galaxies within r_{200} , $E(z) = [\Omega_{\Lambda} + (1+z)^3\Omega_m]^{1/2}$, $A_{1D} = 1177 \pm 4.2 \text{ km s}^{-1}$, and $\alpha = 0.0364 \pm 0.002$ (Sifón et al. 2016). Using the velocity dispersion measurement of Ruel et al. (2014) for ACT-CL J0245–5302, $\sigma_{200} = 1245 \pm 210 \text{ km s}^{-1}$, we estimate a virial mass $M_{200} = (14.48 \pm 0.82) \times 10^{14}M_{\odot}$ for this cluster.

This analytical procedure is expected to provide a reasonable estimate of the magnification produced by clusters with approximately spherical dark matter mass density profiles. However, it is not appropriate for the case of ACT-CL J0102–4915, which is undergoing a major merger between two clumps with mass ratio 2:1 (Menanteau et al. 2012) that form a very elongated lens with axis ratio ~ 5.5 (Zitrin et al. 2013). Hence, for sources in the field of ACT-CL J0102–4915, we obtain magnification factors directly from lensing maps generated by

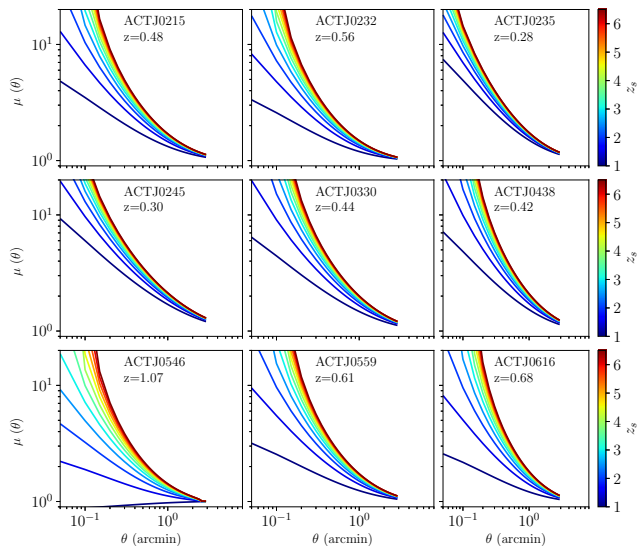


Figure 4. Gravitational magnification vs. radius for clusters with virial mass and radius measured by Sifón et al. (2013). In each case, we calculate the expected magnification as a function of angular distance to the cluster’s center for a range of source redshifts from $z_s=1.0$ to $z_s=7.0$, in steps of $\Delta z_s = 0.5$.

Zitrin et al. (2013) at the corresponding source redshifts (private communication).

The results of our lensing models for all LASCAR clusters except ACT–CL J0102–4915 are shown in Figure 4, where we plot the resulting $\mu(\theta)$ curves for a set of source redshifts (z_s) from $z_s = 1.0$ to $z_s = 7.0$, so as to cover the full range expected for the SMG population. We find that in general the maximum magnification factor can reach up to $\sim 10 - 11$ close to the cluster’s core, but at radii larger than ~ 4 arcmin the magnification becomes negligible. We also see that for a given radius, sources at higher redshifts are more strongly lensed, but this dependence becomes less significant beyond $z_s \sim 3$. For very distant sources, the magnification factor is not strongly influenced by redshift, i.e., sources at $z_s = 4.0$ and $z_s = 7.0$ will experience similar lensing.

To estimate the magnification factor for each source, we use the models described above, the cluster-centric angular distances θ given in Table 5, and the photometric redshifts calculated from our SED modeling. For sources with no photometric redshift estimates, we assume $z_s = 2.8 \pm 0.7$, the median value for our sample with robust counterpart identifications. The propagated errors due to uncertainties in the virial mass and radius and in the source and cluster (z_c) redshifts were calculated separately and added in quadrature; for each variable we performed 1000 Monte Carlo simulations using random values generated from a Gaussian probability distribution with mean and standard deviation equal to

the experimental measurement and error. Mathematically, from the random simulations we obtain the individual errors $\sigma_{M_{200}}$, $\sigma_{r_{200}}$, σ_{z_c} and σ_{z_s} , and sum them in quadrature to calculate the total error σ_{total} .

We tested the reliability of our magnification estimates by performing a similar analysis for cluster MACSJ1115.8+0129, which has been observed in 16 bands with *HST* by the Cluster Lensing And Supernova survey with *Hubble* (CLASH; Postman et al. 2012) and also has a strong-lensing model (Zitrin et al. 2015). We use the CLASH model best-fit mass for MACSJ1115.8+0129 as input and calculate the expected magnification curve ($\mu(\theta)$ vs. θ) for a source at $z = 2.8$ (our median sample redshift) following the algorithm described above. We obtain an analogous curve for the Zitrin et al. (2015) model by calculating the azimuthally-averaged magnification factor at each projected radius; in Figure 5 we plot both results. We find that, for equal virial mass, the magnifications predicted by our analytical algorithm are underestimated by a factor up to ~ 40 within the inner arcminute compared to those derived from the detailed strong lensing analysis, but at radii beyond $\sim 1.2'$ the discrepancies are reduced to $\sim 10\%$. The reported discrepancies in the inner region may be explained by the differences in the assumed density profile (elliptical vs. spherical NFW), and also by the fact that the CLASH model includes the dark matter contributions of individual galaxies in the cluster, such that the total density profile steepens towards the center, thus boosting the lensing magnification (Zitrin et al. 2015). This is a more realistic representation of the cluster’s mass distribution, so we can conclude that for background sources detected at projected radii under $\sim 1.2'$, estimation of magnification factors based solely on a cluster’s virial mass is insufficient, and lens modeling based on high-resolution imaging is required to derive intrinsic luminosities. Since such data are not available at present for most clusters in our sample, for the following number counts analysis we exclude sources located at $\theta \leq 1.2'$. As seen in Table 5, this criterion affects 6 sources in our catalog (ACTJ0215–3, ACTJ0235–2, ACTJ0245–2, ACTJ0546–2, ACTJ0546–8, and ACTJ0616–2).

6.4. Number counts

With the final catalog of de-magnified sources, we can construct the integral number counts for LASCAR. In total, we detect 49 SMGs, but we exclude from this analysis 6 sources (listed above) in the fields of clusters ACTJ0235, ACTJ0245, ACTJ0546 and ACTJ0616 with cluster-centric radii under $1.2'$, for which we are currently unable to derive accurate intrinsic flux den-

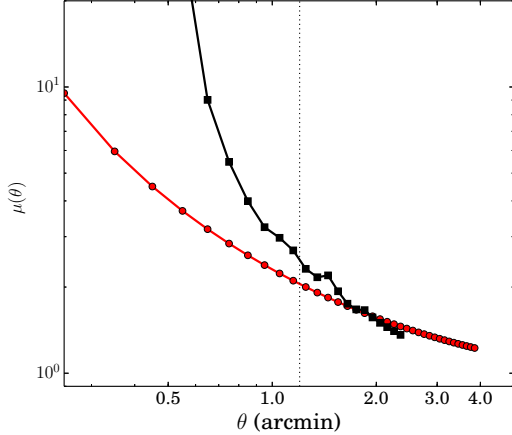


Figure 5. Comparison of magnification radial profiles predicted by the CLASH lensing model for cluster MACS J1115.8+0129 (black, squares) and our calculations (red, circles), for a background source at $z = 2.3$, the median redshift of a purely submillimeter flux-limited SMG sample as predicted by Chapman et al. (2005). The vertical dotted line at $\theta = 1.2'$ marks the radius where discrepancies between the two models are reduced to $\sim 10\%$.

sities. We also identify ACTJ0235–3 as a foreground galaxy, so the reported number counts are based on a total of 42 sources detected over 10 fields. We bin the sources by intrinsic flux density, and use the completeness and magnification estimates obtained in Sections 5 and 6.3 to account for undetected sources and to calculate the total effective area surveyed by our LABOCA maps. Bin centers are defined to match the minimum and maximum de-magnified flux densities in our source catalogs, and we use a constant logarithmic bin width $\Delta \log_{10}(S_{870}) = 0.1$.

Completeness corrections for each cluster field are based on the curves presented in Figure 2, which indicate the fractions of successful detections relative to the total number of sources at different flux densities, which we refer to as C . We assume that for each detection at observed flux density S_{obs} , there are $N_{\text{undet}} = C^{-1} - 1$ undetected sources, randomly located across the LABOCA map. To estimate the distribution of *intrinsic* flux densities for these missing objects, we add N_{undet} point sources with S_{obs} and uniform spatial distribution to each cluster map, obtain their expected magnifications using the lensing curves in Figure 4, and calculate their intrinsic flux densities. The resulting catalogs of simulated sources are then binned in the same way as the detected SMGs; the process is repeated 1000 times to obtain average number counts for the undetected point source population. Finally, both sets of number counts

(detected and undetected) are added to obtain the final completeness-corrected number counts over all fields.

The total effective area surveyed by our submillimeter maps depends on the target intrinsic flux density of point sources, which are magnified by the foreground clusters. In the lensing formalism, the image area is calculated as $A_{\text{image}} = \mu A_{\text{source}}$, where A_{source} is the area in the source plane and μ the magnification factor. For each intrinsic flux density S_{int} we can calculate the minimum magnification μ_{min} required so that the observed flux density S_{obs} is above the 4σ detection threshold, $\mu_{\text{min}} = 4\sigma/S_{\text{int}}$. Hence, the effective area where sources of flux density S_{int} can be detected corresponds to the set of pixels where $\mu \geq \mu_{\text{min}}$; we use the magnification maps in Figure 4 to determine this region for each cluster assuming a median source redshift $z = 2.8$, and calculate the effective source plane area as

$$A_{\text{source}}(S_{\text{int}}) = \sum_{\mu_i \geq \mu_{\text{min}}} A_{\text{pix}}/\mu_i \quad (4)$$

where i runs over all pixels in the detection map minus the inner $1.2'$ where magnification estimates are uncertain (except for ACTJ0102), and $A_{\text{pix}} = 12.96 \text{ arcsec}^2$ is the image pixel area. We then add all clusters' effective areas to obtain the total de-magnified area for the complete survey. The completeness-corrected binned number counts are then divided by this total area. In Figure 6, we show the resulting S_{int} vs. A_{source} curves for each cluster, and the total summed curve for the LASCAR survey.

The uncertainties in number counts were derived from Poisson statistics, which apply when event rates are calculated from small numbers of observed events (Gehrels 1986). Our results are given in Table 6 and plotted in Figure 7. For comparison, we also show the integral number counts from the lensing cluster surveys of Knudsen et al. (2008) and Johansson et al. (2011), from the SCUBA Half-Degree Extragalactic Survey (SHADES; Coppin et al. 2006), from LESS (Weiß et al. 2009), from SCUBA-2 (Hsu et al. 2016), and from the high-resolution ALMA follow-up of LESS (Karim et al. 2013). We find that, for the intrinsic flux density range covered by our survey, results are consistent within uncertainties with previous single-dish surveys conducted in blank fields (e.g., Coppin et al. 2006), towards lensing clusters (Knudsen et al. 2008; Johansson et al. 2011), and combining both cluster and blank fields (Hsu et al. 2016). The exception is the datapoint at $S_{\text{int}} = 6.3 \text{ mJy}$, fainter than the 4σ detection threshold for all cluster, which therefore comprises sources that are necessarily magnified. The discrepancy is possibly due to the uncertainties in our analytical lens models, which

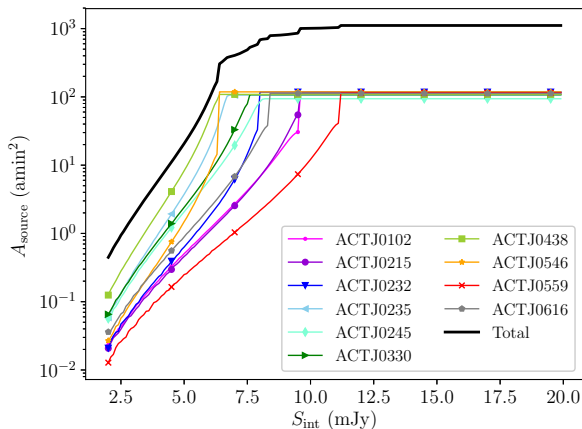


Figure 6. Effective source plane area A_{source} where sources of intrinsic flux density S_{int} can be detected, considering magnification effects. Curves for individual clusters are plotted as indicated in the figure legend, and the solid black curve represents the total summed effective area for the LASCAR survey. Individual cluster curves converge to an effective area equal to the total image area for $S_{\text{int}} = 4\sigma$, when $\mu_{\text{min}} = 1$.

may generally underestimate magnification factors relative to those derived from strong lensing models, as suggested by the comparison presented in Figure 5. If magnification factors are minimally increased across the field, intrinsic flux densities and binned number counts do not vary significantly, but the detectable area A_{source} where $\mu > 4\sigma/S_{\text{int}}$ is increased, thus affecting the number counts per unit area. To test this hypothesis, we repeated our calculations but slightly scaled our analytical magnification maps by a factor ~ 1 . We find that a satisfactory match between our resulting number counts at $S_{\text{int}} = 6.3$ mJy and previous surveys can be reached if all magnification estimates are varied by only $\sim 5\%$, which is within the uncertainties obtained for μ and listed in Table 5.

Compared to number counts obtained by Weiß et al. (2009) for LESS, our results are larger by a factor ~ 2 – 9 depending on the intrinsic flux density, but it has been reported in the literature that bright SMGs and other rest-frame optical populations are underabundant in the ECDFS compared to other deep fields (see Weiß et al. (2009) and references therein). Karim et al. (2013) reported $870 \mu\text{m}$ number counts derived from high resolution ($\sim 1.5''$) ALMA continuum imaging of SMGs detected by LESS, which has revealed that bright SMGs with $S_{870} \gtrsim 12$ mJy are actually resolved into multiple, fainter sources with individual flux densities $\lesssim 9$ mJy (Hodge et al. 2013; Karim et al. 2013). As a result, ALMA integral number counts of Karim et al. (2013) are lower than those of LASCAR and other single-dish

surveys but comparable to the predictions of Weiß et al. (2009) for $S_{870} \lesssim 9$ mJy, declining steeply at higher flux densities. Hence, like other single-dish surveys, LASCAR presumably overestimates the number of intrinsically bright sources behind the sample of ACT galaxy clusters.

7. CONCLUSIONS

The LABOCA/ACT Survey of Clusters at All Redshifts (LASCAR) has obtained $870 \mu\text{m}$ LABOCA and 2.1 GHz ATCA mapping for a set of ten massive SZE-selected galaxy clusters from the ACT southern survey, and *Herschel* PACS and SPIRE data for sample subsets (5 and 6 clusters, respectively), with the aim of studying the properties of the clusters' SZE signals and of the background SMG population from the same dataset. In Lindner et al. (2015) we estimated the levels of radio source and SMG contamination of the SZE signal and constraints on the cluster peculiar velocities using the kinetic SZE effect; in this work we present a study of the submillimeter point sources detected in the fields of the LASCAR targets.

The $870 \mu\text{m}$ LABOCA maps were reduced using a multi-scale iterative pipeline that successfully extracts the extended SZE increment signal and yields point-source sensitivities of ~ 2 mJy beam $^{-1}$. We applied an enhanced matched-filter extraction algorithm to recover 49 sources at the 4σ level, and we used our radio and *Herschel* observations plus existing near-IR and optical data to conduct a detailed analysis of their multi-wavelength properties. First, we used our combined dataset to identify the likely counterparts of the detected SMGs. We find that one corresponds to a foreground galaxy (ACTJ0235–3), four have double radio counterparts, 28 have single radio counterparts, and 16 have no radio counterparts. In the case of SMGs with double radio matches, which could be interpreted as merging or interacting subcomponents of a single SMG (or as double lobes of a radio-loud SMG), we can identify individual counterparts in the near- and far-IR and in the optical imaging, but we cannot disentangle their separate contributions to the emission at 870 , 500 , 350 , and $250 \mu\text{m}$, where they are blended together due to coarser spatial resolutions. For SMGs that have single detections at 2.1 GHz, we can generally determine their correspondence to specific PACS, IRAC, and optical sources, but there are three cases (ACTJ0235–1, ACTJ0235–5, and ACTJ0330–1) in which the radio beam encompasses two or more IRAC/optical sources, so we can only identify a tentative counterpart at our shortest wavelengths. For the remaining SMGs that are

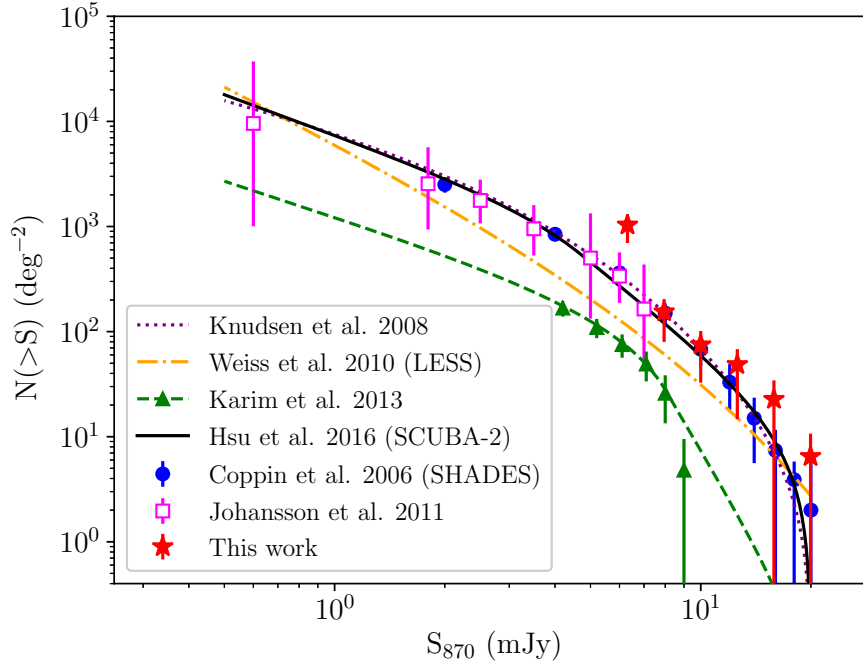


Figure 7. Integral number counts for submillimeter sources detected behind 13 galaxy clusters. The plotted results consider in total 42 background sources detected at cluster-centric radii larger than $1.2'$. Our counts have been corrected for completeness and gravitational magnification, using the results from Sections 5 and 6.3 respectively. For comparison, we also show previous results from Hsu et al. (2016); Karim et al. (2013); Johansson et al. (2011); Knudsen et al. (2008); Weiß et al. (2009), and Coppin et al. (2006). Line plots correspond to the best-fitting Schechter functions for each dataset.

not detected at the 4σ level in our 2.1 GHz maps, we analyze all *Herschel*, IRAC, and optical sources located within the LABOCA beam and try to select candidate counterparts based on PACS detections, and on comparison of near-IR colors to previous SMG observations. We succeed in identifying tentative counterparts for 9 of these systems.

For 34 sources with secure (25) and tentative (9) matches at different wavelengths, we estimate photometric redshifts through minimum- χ^2 fitting of template SEDs from the library of Michałowski et al. (2010) and obtain values from $z \sim 1.1$ to $z \sim 4.9$. For sources with tentative counterpart identifications, the photometric redshift estimates still need to be confirmed through high-resolution continuum mapping at millimeter or submillimeter wavelengths, which is the only unbiased method for unequivocal matching to sources detected in near-IR and optical imaging. For LASCAR SMGs with counterparts classified as “secure”, we obtain a photometric redshift distribution whose median $z = 2.8^{+2.1}_{-1.7}$ is consistent with results in the literature. We find an excess of sources at redshifts $z > 3$ relative to previous studies, although we note that with the limited number of bands currently available for SED modeling (only 4 in cases where only radio and IRAC counterparts

are identified), estimated photometric errors are bound to be significant, of order $\Delta z \sim 1.0$.

Since our detected SMGs lie behind galaxy clusters, they are expected to be gravitationally lensed. For sources in the field of ACT-CL J0102–4915 we use magnification estimates from the strong-lensing model of Zitrin et al. (2013), and for the remaining clusters we apply analytical models to estimate the magnification factor at the position of each SMG using cluster virial mass measurements in the literature. The resulting amplifications should have 10% or better accuracy for sources outside $\sim 1.2'$ of the cluster’s core; in order to determine accurate amplifications for all sources, it is necessary to obtain *HST* high-resolution optical/infrared imaging that can be used for strong lensing modeling of the dark matter mass distribution.

We use the final de-magnified flux densities to construct the integral number counts for LASCAR, excluding from this analysis six sources located at cluster-centric radii under $1.2'$, for which amplification factors are not well determined, and one additional object identified as a foreground galaxy. Our results are in good agreement with those of previous submillimeter surveys in the overlapping flux density ranges. Comparison at fainter flux densities is hindered however by the lack

Table 6. Integral number counts at $870\ \mu\text{m}$.

S_{870} (mJy)	$N(> S_{870})$ (deg^{-2})
6.3	1035^{+339}_{-252}
7.9	154^{+75}_{-49}
10.0	75^{+42}_{-27}
12.6	49^{+34}_{-20}
15.8	23^{+26}_{-12}
20.0	7^{+19}_{-4}

NOTE—Counts are based on 42 foreground SMGs detected at cluster-centric radii $\geq 1.2'$. Calculations include corrections for gravitational magnification and completeness.

of more precise strong-lensing modeling of the clusters' central regions, where magnifications are expected to be highest and detected SMGs may prove to be intrinsically very faint. Towards the bright end, LASCAR number counts are consistent with those of previous single-dish surveys, but likely overestimate the number of sources with $S_{870} \gtrsim 9$ mJy compared to high-resolution ALMA observations, which indicate that $\sim 30 - 50\%$ of sources with single-dish flux density measurements above this limit may resolve into multiple, fainter components. High-resolution ALMA continuum mapping of SMGs detected in LASCAR is required to determine their single or multiple component nature, confirm and refine identification of near-IR and optical counterparts, and thus improve photometric redshift estimates and number counts; such data have been obtained by our team for a selection of LASCAR sources and will be reported in the near future.

We thank the anonymous referee for useful comments that have helped improved this paper. We also thank John Wu for his valuable comments on the paper; and Mauricio Carrasco and Adi Zitrin for providing lensing magnification maps for ACT-CL J0102-4915. P.A. acknowledges support from CONICYT through grant FONDECYT Iniciación 11130590, and A.J.B. acknowl-

edges support from NSF grant AST-0955810. R.D. acknowledges support from CONICYT through grants FONDECYT 1141113, Anillo ACT-1417 and BASAL PFB-06 CATA. J.P.H. acknowledges the hospitality of the Flatiron Institute which is supported by the Simons Foundation. M.L. is partially supported by CNPq and FAPESP.

ACT operates in the Parque Astronómico Atacama in northern Chile under the auspices of the Programa de Astronomía de la Comisión Nacional de Investigación Científica y Tecnológica de Chile (CONICYT). This work was supported by the U.S. National Science Foundation through awards AST-0408698 and AST-0965625 for the ACT project, and PHY-0855887, PHY-1214379, AST-0707731, and PIRE-0507768 (award No. OISE-0530095). Funding was also provided by Princeton University, the University of Pennsylvania, and a Canada Foundation for Innovation (CFI) award to UBC. Computations were performed on the GPC super-computer at the SciNet HPC Consortium. SciNet is funded by the CFI under the auspices of Compute Canada, the Government of Ontario, the Ontario Research Fun-Research Excellence, and the University of Toronto. APEX is operated by the Max-Planck-Institut für Radioastronomie, the European Southern Observatory, and the Onsala Space Observatory.

APPENDIX

A. NOTES ON INDIVIDUAL SOURCES

In the following paragraphs, we report some relevant details on counterpart identification, SED modeling and estimation of photometric redshifts for each SMG in the LASCAR catalog. In Figures 8 to 17 we present $30'' \times 30''$ multi-wavelength postage stamps at the locations of the $870\ \mu\text{m}$ sources, and in Table 7 we list the corresponding multi-wavelength flux densities. Finally, in Figure 18 we show SED template fits for sources with robust and tentative

counterpart identifications.

ACTJ0102–1: This source stands out as the brightest SMG in our catalog, with $S(870) = 33.9 \pm 1.4$ mJy. It lies at a projected cluster-centric radius of $34.82''$, so it is likely magnified by the cluster’s gravitational potential. Within the LABOCA beam, we detect a single radio counterpart that has matching emission at $100/4.5/3.6 \mu\text{m}$ and in the optical. The best-fit SED model suggests $z_{\text{phot}} \sim 4.5$.

ACTJ0102–2: There are no 4σ radio counterparts within the LABOCA beam, but the source is detected in SPIRE bands and we identify a tentative IRAC counterpart. The high noise of PACS imaging at the location of this source hinders detection of a $100/160 \mu\text{m}$ counterpart. Assuming the IRAC match is correct, we estimate $z_{\text{phot}} \sim 4.5$, but deeper radio imaging or high-resolution submillimeter continuum mapping is required to confirm it.

ACTJ0102–3: This source has a radio/IRAC/optical counterpart and is detected as well in SPIRE bands, but not at $100/160 \mu\text{m}$. The observed SED and upper flux density limits at $100/160 \mu\text{m}$ are consistent with $z_{\text{phot}} \sim 4.2$.

ACTJ0102–4: We identify a single radio/IRAC counterpart, which is detected in all SPIRE bands. The source is located close to the border of the cluster’s PACS and optical imaging, so we are not able to determine the existence of a counterpart at these wavelengths. SED modeling points to $z_{\text{phot}} \sim 2.0$.

ACTJ0102–5: This source is detected as a single object at all wavelengths for which data are available; we obtain a good fit from the radio to optical bands for a low $z_{\text{phot}} \sim 1.1$.

ACTJ0215–1: This source has no radio detection; peaks visible in the 2.1 GHz stamp in Figure 9 are consistent with noise. Two IRAC sources are found within the LABOCA search radius, but both have $S_{4.5}/S_{3.6}$ colors inconsistent with SMG templates. We are therefore unable to select a tentative counterpart.

ACTJ0215–2: There is no radio detection at the 4σ level, but we identify a single IRAC counterpart candidate within the LABOCA beam. The source lies outside the cluster’s optical mapping. With only two tentative photometric points besides the $870 \mu\text{m}$ measurement, we are unable to estimate a photometric redshift.

ACTJ0215–3: As for ACTJ0215–2, we have no 4σ radio detection and can only identify a tentative IRAC counterpart that lies close to the $870 \mu\text{m}$ centroid and has a flux density ratio $S_{4.5}/S_{3.6} = 1.1$, consistent with previous SMG near-IR observations.

ACTJ0215–4: We do not detect a significant radio counterpart, and furthermore we are not able to select a single counterpart candidate among several IRAC/optical sources within the LABOCA beam. Our data are thus insufficient for SED modeling and estimation of a photometric redshift.

ACTJ0232–1: A radio counterpart matches a very faint IRAC $3.6/4.5 \mu\text{m}$ source, but is undetected in the optical. These measurements are consistent with $z_{\text{phot}} \sim 4.5$.

ACTJ0232–2: Like ACTJ0232–1, this source is detected in radio imaging and faintly in the IRAC bands, but not in optical bands. We obtain a best-fit $z_{\text{phot}} \sim 2.8$.

ACTJ0232–3: We see no significant radio detection but identify two IRAC sources located within the LABOCA beam that may constitute a double-component counterpart to the submillimeter detection. We cannot determine the components’ individual contributions to the submillimeter counterpart or model their SEDs.

ACTJ0232–4: This source has a strong radio counterpart that matches a single IRAC $4.5/3.6 \mu\text{m}$ source. There is no optical coverage at the location of this SMG, but we estimate $z_{\text{phot}} \sim 1.5$.

ACTJ0232–5: We detect a single radio source exactly on the edge of the LABOCA beam with $P_C = 0.03$, which is also detected in IRAC bands and has $S_{4.5}/S_{3.6} = 1.33$ consistent with an SMG. We estimate $z_{\text{phot}} \sim 1.7$.

ACTJ0235–1: Multi-wavelength imaging reveals that this source may correspond to a complex multi-component system. We detect one radio counterpart in the 2.1 GHz 4σ catalog, but visual inspection of ATCA and IRAC imaging suggests that the submillimeter emission may actually be resolved into three sources aligned in a north-east direction. The northernmost component is on the edge of the LABOCA beam and is seen faintly in radio and IRAC imaging, but it is beneath the detection thresholds of our catalogs. The central component is a significant radio/IRAC detection, while the south-east component is also barely within the LABOCA beam, but is detected at high S/N in PACS and IRAC imaging. We also detect SPIRE 500/350/250 μm emission that appears to be centered closer to the south-east component. At the depth and resolution of our imaging, we are unable to disentangle the submillimeter, radio, and far-IR emission of each individual component, so we cannot estimate the photometric redshift of the SMG. High-resolution submillimeter continuum mapping is required to correctly identify the source of the 870 μm emission and correlate it with sources detected at shorter wavelengths and in radio mapping.

ACTJ0235–2: There are no radio detections within the LABOCA beam, but the source is detected in all *Herschel* bands. At 100 μm we detect two sources, which are blended together in the broader beam at 160 μm . The north 100 μm source matches an IRAC/optical counterpart that has properties consistent with the SMG population and is selected as a tentative counterpart. Since we are unable at this point to disentangle the contribution of the counterpart candidate to the emission measured at 500, 350, 250 and 160 μm , only the 100 μm , IRAC and optical flux densities were used in SED modeling, which yields a tentative $z_{\text{phot}} \sim 2.9$.

ACTJ0235–3: This source coincides with the position of the foreground galaxy ESO 198-G021, which has a redshift of $z = 0.018$ as reported in the 6dF Galaxy Survey Database (Jones et al. 2009); it is bright in the optical and near-IR, but much fainter at 2.1 GHz. The emission in SPIRE, PACS, IRAC, and optical bands is dominated by this galaxy, but we also detect a radio source that lies within the LABOCA beam offset from the centroid of ESO 198–G021.

ACTJ0235–4: No radio counterpart is seen in our ATCA mapping, but we detect emission in all SPIRE bands, at 100 μm , and in IRAC/optical imaging. We consider this source a plausible counterpart to the SMG detected at 870 μm ; we perform SED modeling and estimate $z_{\text{phot}} \sim 4.0$.

ACTJ0235–5: This source has a clear radio counterpart that overlaps two IRAC sources and also matches closely the location of a SPIRE 250/350/500 μm source. Although we also detect a PACS 100/160 μm source within the LABOCA beam, its centroid lies outside the ATCA beam, so it is likely not associated with the 870 μm /SPIRE/IRAC emission. Both IRAC sources have near-IR colors $S_{4.5}/S_{3.6} \sim 1.4$ comparable to previous observations for SMGs (Hainline et al. 2009), so we are unable to select a single one as the SMG counterpart. If we choose the IRAC galaxy closest to the 2.1 GHz centroid, the estimated redshift is $z_{\text{phot}} \sim 3.7$, but we note that we may be looking as well at a double system. There is no optical coverage at the location of this source.

ACTJ0245–1: We do not detect a radio or PACS counterpart. However, the source is seen in the SPIRE bands, and we identify an IRAC counterpart candidate that is not seen in the optical imaging. For the tentative IRAC counterpart, we estimate $z_{\text{phot}} \sim 4.0$, which corresponds to an SED fit that is consistent with PACS/radio upper limits.

ACTJ0245–2: This source is detected in the SPIRE bands and has a radio counterpart that matches an IRAC source, but is undetected in optical. The IRAC counterpart is one of four sources found inside the LABOCA beam, all of which are blended together at the resolution of PACS 100/160 μm imaging. Hence, although the SMG has detectable 100/160 μm emission, we are not able to determine its individual flux density due to source blending. We do not include these bands in SED modeling, and obtain a good fit at $z_{\text{phot}} \sim 2.1$ to the 870 μm , SPIRE, radio, and IRAC photometry.

ACTJ0245–3: This source has a single radio/SPIRE/IRAC counterpart but is undetected in PACS and optical imaging. Our SED modeling implies redshift $z_{\text{phot}} \sim 3.8$ and is consistent with PACS 100/160 μm upper limits derived

from non-detections at the 3σ level.

ACTJ0330–1: In our ATCA 2.1 GHz catalog we identify a radio counterpart that matches the location of an IRAC source. Assuming these are the radio/near-IR counterparts for our SMG, we estimate $z_{\text{phot}} \sim 3.0$. However, visual inspection of the radio and IRAC imaging shows that the selected counterpart is accompanied by two fainter IRAC sources that may be blended together in our radio mapping, forming an elongated feature that is fainter than the detection limit of our radio catalog. Hence, the detected SMG may correspond to a multiple system; confirmation can only be achieved with high-resolution submillimeter mapping.

ACTJ0330–2: A single radio counterpart matches the location of the only IRAC source within the LABOCA beam, which we thus identify as the likely near-IR counterpart. SED fits to these four data points give $z_{\text{phot}} \sim 3.2$.

ACTJ0330–3: As for ACTJ0330–2, we identify a single radio/IRAC counterpart and estimate a photometric redshift $z_{\text{phot}} \sim 1.7$.

ACTJ0438–1: There are no radio or PACS counterparts detected within the LABOCA beam, but we do detect the source in the SPIRE bands. However, the centroid of the SPIRE emission is located close the edge of the beam, and it is unclear whether it is associated with the $870\ \mu\text{m}$ source, or with a PACS $100/160\ \mu\text{m}$ source located just outside the beam. We identify a tentative IRAC counterpart, which is undetected in the optical. Adopting the SPIRE and IRAC counterparts, we obtain a tentative $z_{\text{phot}} \sim 3.4$.

ACTJ0438–2: This SMG is detected in SPIRE and PACS $100\ \mu\text{m}$ imaging, but not at 2.1 GHz or $160\ \mu\text{m}$. The PACS $100\ \mu\text{m}$ detection matches an IRAC counterpart. Our SED fit indicates $z_{\text{phot}} \sim 3.2$ and is consistent with a radio upper flux density limit corresponding to our 4σ detection threshold.

ACTJ0438–3: The source’s radio and far-IR emission is lower than the thresholds of our ATCA and *Herschel* catalogs, so we cannot pinpoint the location of the $870\ \mu\text{m}$ source. We detect three IRAC counterpart candidates within the LABOCA beam but are unable to select one of them as the SMG counterpart.

ACTJ0438–4: Two radio sources lie close to the search radius; we denote them ACT0438–4A (north) and ACT0438–4B (south). ACT0438–4A is detected in PACS, IRAC, and optical imaging, while ACT0438–4B is only detected at 4.5 and $3.6\ \mu\text{m}$. There is no SPIRE counterpart to the submillimeter emission.

ACTJ0438–5: The source is detected in radio imaging, in all SPIRE bands, and at $100\ \mu\text{m}$, and based on the precise radio positioning we are able to identify as well an IRAC counterpart. SED modeling of these data result in a $z_{\text{phot}} \sim 3.5$.

ACTJ0438–6: This source is detected in radio mapping as a double system, and we are able to identify a PACS/IRAC counterpart for each component. We identify the northern radio counterpart as source ACTJ0438–6A, which is also detected at $100/4.5/3.6\ \mu\text{m}$ and in the optical. The southern radio source is denoted ACTJ0438–6B and is detected in all PACS and IRAC bands. We also detect a SPIRE $500/350/250\ \mu\text{m}$ source that is centered closer to the location of ACTJ0438–6B.

ACTJ0438–7: There are no radio, SPIRE, or PACS counterparts above the defined detection thresholds. Out of three IRAC sources located inside the LABOCA beam, only one has an $S_{4.5}/S_{3.6}$ ratio close to that expected for SMGs, so we single it out as a counterpart candidate. However, accurate positioning at radio or submillimeter wavelengths is required to confirm this possible association.

ACTJ0438–8: For this SMG we detect two radio counterparts within the LABOCA beam, denoted ACTJ0438–8A (west) and ACTJ0438–8B (east), which respectively match IRAC sources. We also detect SPIRE and PACS sources, but in these cases the emission from both counterparts is blended together due to the lower spatial resolution compared to radio and near-IR imaging. Only ACTJ0438–8A is detected in the optical. Since we are unable to disentangle the

contribution of each source to the submillimeter and far-IR emission, we cannot model their SEDs individually.

ACTJ0546–1: A radio counterpart matches a SPIRE and IRAC source, but is undetected at PACS wavelengths and has no optical imaging coverage. SED fitting based on radio, SPIRE, and IRAC measurements suggest a high $z_{\text{phot}} \sim 4.9$.

ACTJ0546–2: This source is detected at all wavelengths except the optical, but at the higher resolutions of the IRAC and optical imaging we find that the radio counterpart may actually encompass at least two of three neighboring galaxies that are blended in the PACS and ATCA beams. Based on the location of the radio source and the optical non-detection, we propose that the source located at the center of this system is the correct SMG counterpart, and in fact we find a good SED fit with $z_{\text{phot}} \sim 1.9$ considering only the submillimeter, SPIRE, and IRAC photometry for the source indicated in Figure 15. However, if we try to fit as well flux densities measured for the PACS 100(160) μm source detected within the LABOCA beam, we are unable to reproduce the observed radio flux density, which further supports the hypothesis that the PACS detections actually correspond to two or more near-IR/optical sources blended by the $7.2''(12'')$ beams.

ACTJ0546–3: The submillimeter source has a single radio/SPIRE/PACS/IRAC counterpart, but is undetected at optical wavelengths. We infer $z_{\text{phot}} \sim 2.2$.

ACTJ0546–4: We identify a single radio counterpart that is detected in all *Herschel* bands except 160 μm , and in IRAC imaging, but not in the optical. SED best-fit templates are consistent with the 160 μm upper density limit and result in $z_{\text{phot}} \sim 4.5$.

ACTJ0546–5: A single radio counterpart matches PACS and IRAC emission, but is too faint for significant detection in the optical and does not have a SPIRE counterpart. The best-fit redshift is $z_{\text{phot}} \sim 2.7$.

ACTJ0546–6: The submillimeter emission has a double radio counterpart aligned in the north-south direction; we denote as ACTJ0546–6A the radio source located on the north edge of the LABOCA beam and ACTJ0546–6B the southern source. Both are detected in PACS and IRAC bands, but not in the optical. We also identify a 500/350/250 μm source that likely corresponds to the combined emission from both sources blended together in the SPIRE beams, although its centroid is located closer to ACTJ0546–6A.

ACTJ0546–7: The location of this source falls outside PACS and optical imaging, but we identify a single radio/SPIRE/IRAC counterpart. We derive $z_{\text{phot}} \sim 3.2$.

ACTJ0546–8: The source has no radio counterpart but is detected in SPIRE bands and at 100 μm . However, the PACS counterpart does not match the location of any of the IRAC/optical sources found within the LABOCA beam, so we cannot identify a candidate counterpart in these bands. Given the limited number of photometric data points, we can venture an estimate $z_{\text{phot}} \sim 2.3$, but the SED fit is very poorly constrained towards the blue extreme.

ACTJ0546–9: We detect a single radio counterpart that matches 100 μm and IRAC detections but is not recovered in our 160 μm or optical catalogs. We estimate its photometric redshift is $z_{\text{phot}} \sim 2.1$.

ACTJ0546–10: We identify a radio counterpart close to the edge of the LABOCA beam that matches an IRAC source. Although we detect some 100/160 μm emission, this may be associated to a SPIRE source located just outside the LABOCA beam rather than to the radio source. The observed photometry matches the SED of an SMG at $z_{\text{phot}} \sim 3.2$.

ACTJ0546–11: We detect a single radio counterpart that matches an IRAC source, but there are no significant SPIRE detections within the LABOCA beam. This SMG lies close to the edge of the PACS image for the cluster ACTJ0546, and we are thus unable to determine the existence of a 100/160 μm match due to increased noise. Optical imaging does not cover the source's location either. Observed photometry is consistent with SED templates of SMGs

at $z_{\text{phot}} \sim 1.9$.

ACTJ0559–1: We identify a strong radio source that matches the location of a single faint IRAC source. There is no optical coverage at the source’s location. Based on this limited photometry, this SMG is expected to lie at $z_{\text{phot}} \sim 2.9$.

ACTJ0616–1: This source has a radio counterpart that accurately matches the position of an IRAC source, but the source’s location is not covered by our optical imaging. We estimate a photometric redshift $z_{\text{phot}} \sim 1.1$.

ACTJ0616–2: There is no 4σ radio detection, but we identify a tentative IRAC counterpart with $S_{4.5}/S_{3.6} \sim 1.46$, consistent with the SMG population. These data are insufficient for SED modeling.

ACTJ0616–3: The source is undetected at 2.1 GHz; we detect several IRAC/optical sources within the LABOCA beam, but are unable to select a probable counterpart.

ACTJ0616–4: This source has a single radio/IRAC counterpart, and SED fitting to the available data points allows us to estimate $z_{\text{phot}} \sim 3.9$.

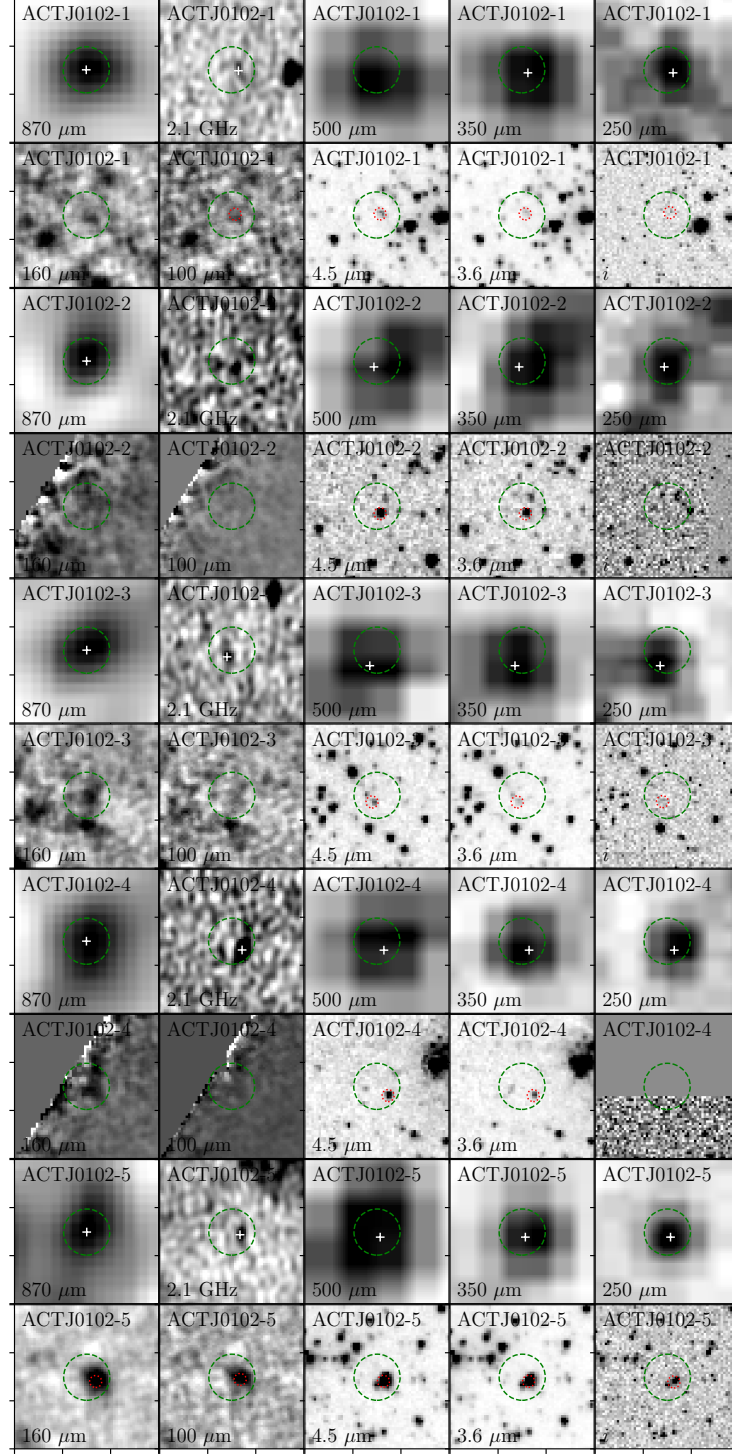


Figure 8. Counterpart identification for SMGs detected in the field of cluster ACTJ0102. For each SMG, we present multi wavelength $60'' \times 60''$ postage stamps centered on the position of the LABOCA source given in Table 5. Ticks are located every $10''$. Dashed circles represent the $19.6''$ FWHM LABOCA beam. The centroids of the LABOCA source and of radio (2.1 GHz) and SPIRE (500/350/250 μm) counterparts are indicated by white crosses. In PACS (160/100 μm), IRAC (4.5/3.6 μm), and optical (i) stamps, the selected counterpart or counterpart candidate (see text in Appendix A) is indicated by a red dotted circle. Spatial resolutions for each band are: $19.2''$ (870 μm), $4''$ (2.1 GHz), $35.0''$ (500 μm), $23.9''$ (350 μm), $17.6''$ (250 μm), $13.0''$ (160 μm), $6''$ (100 μm), $2.5''$ (4.5 and 3.6 μm), and $0.24''$ (optical). North is up and East is left.

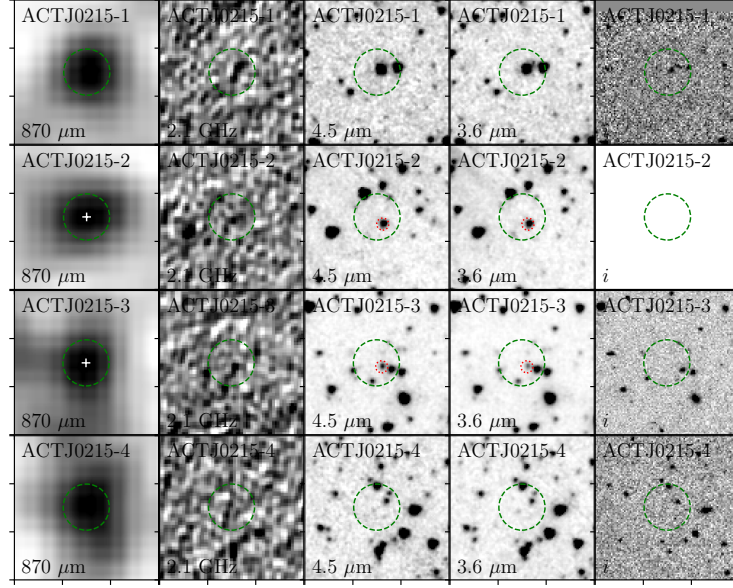


Figure 9. Counterpart identification for SMGs detected in the field of cluster ACTJ0215.

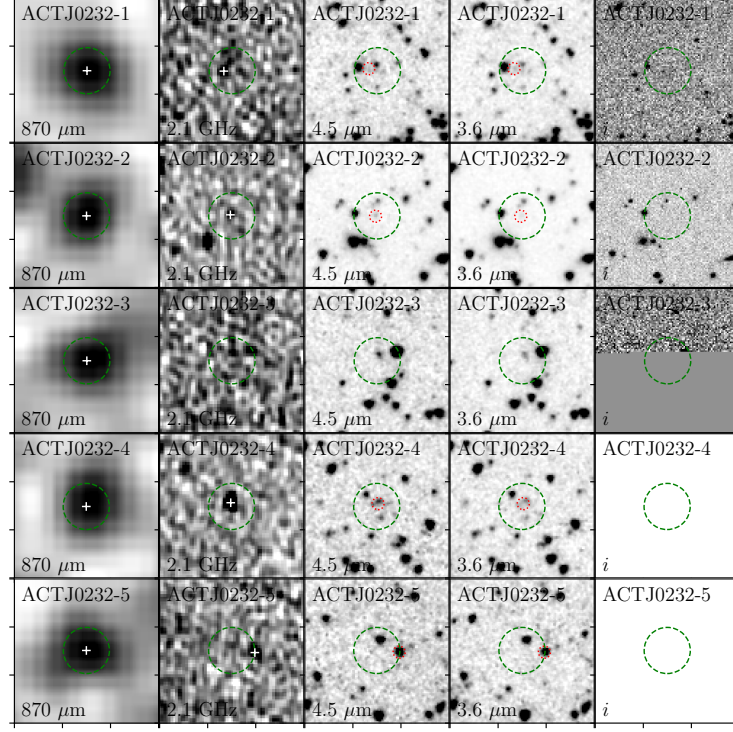


Figure 10. Counterpart identification for SMGs detected in the field of cluster ACTJ0232.

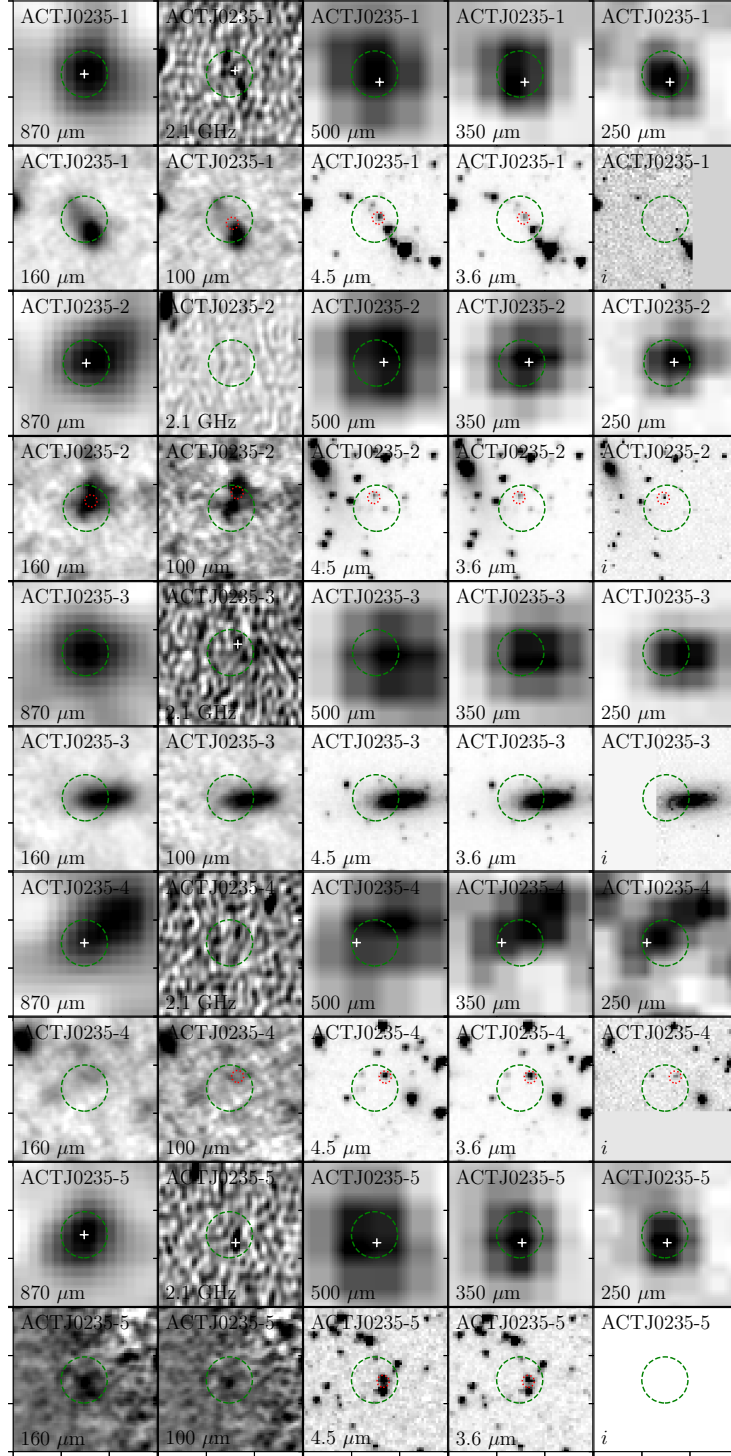


Figure 11. Counterpart identification for SMGs detected in the field of cluster ACTJ0235.

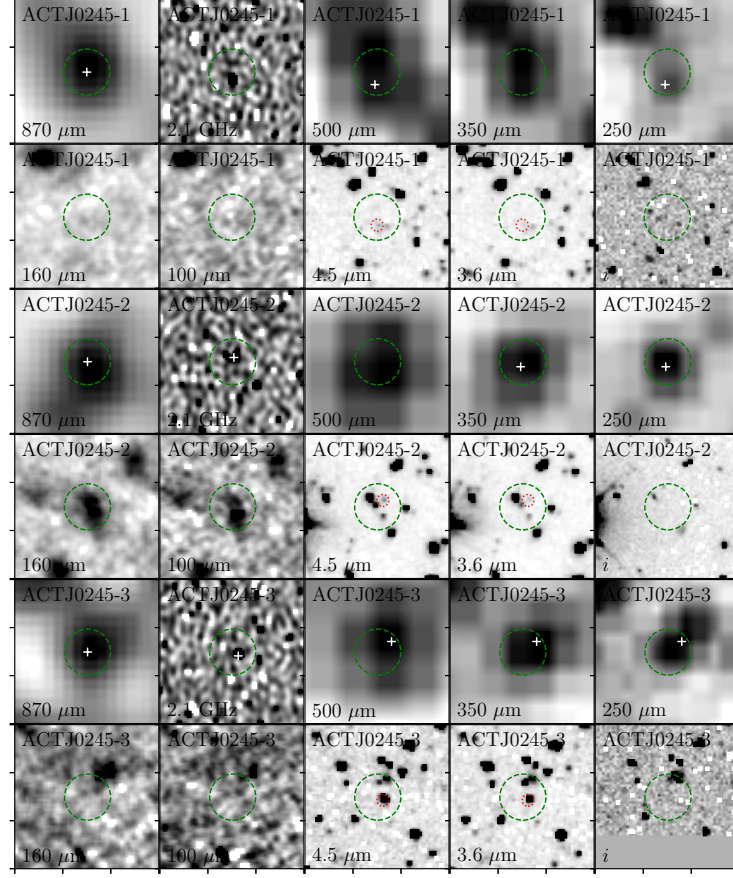


Figure 12. Counterpart identification for SMGs detected in the field of cluster ACTJ0245.

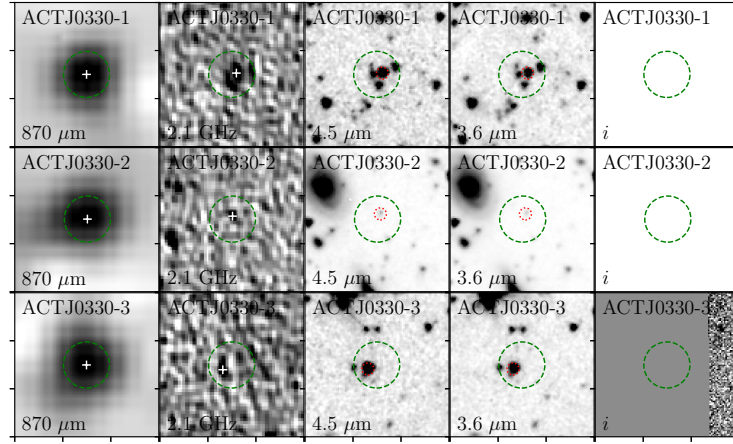


Figure 13. Counterpart identification for SMGs detected in the field of cluster ACTJ0330.

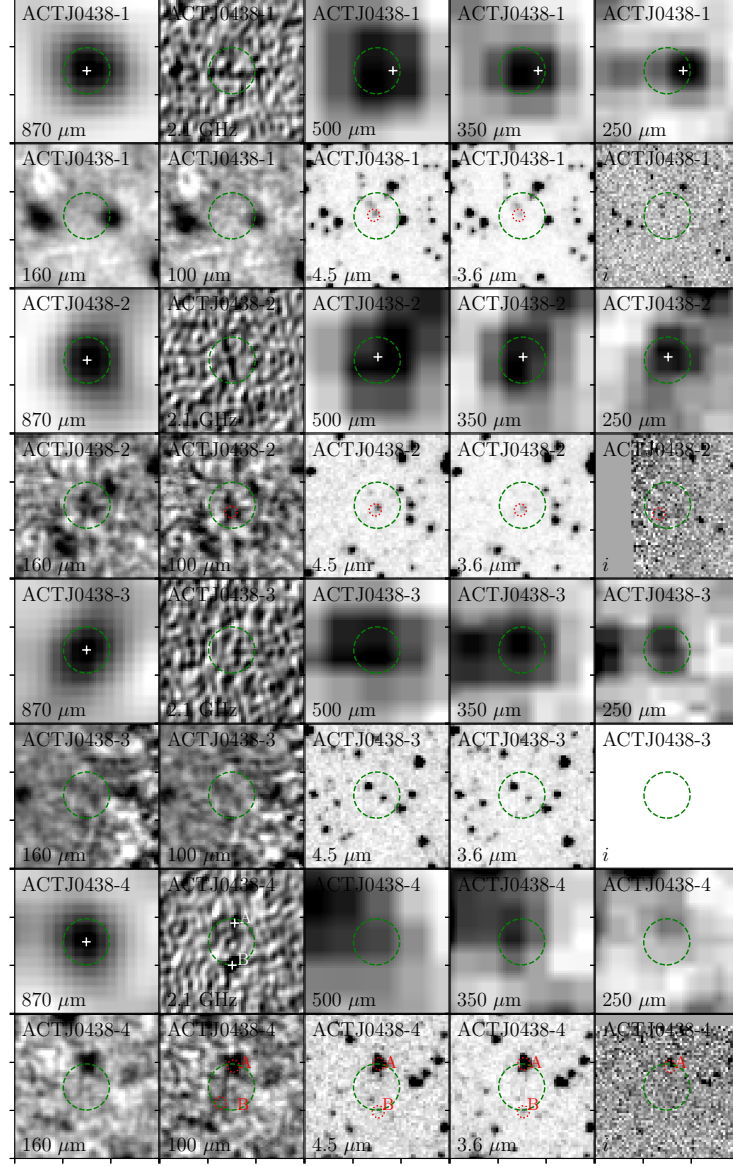


Figure 14. Counterpart identification for SMGs detected in the field of cluster ACTJ0438.

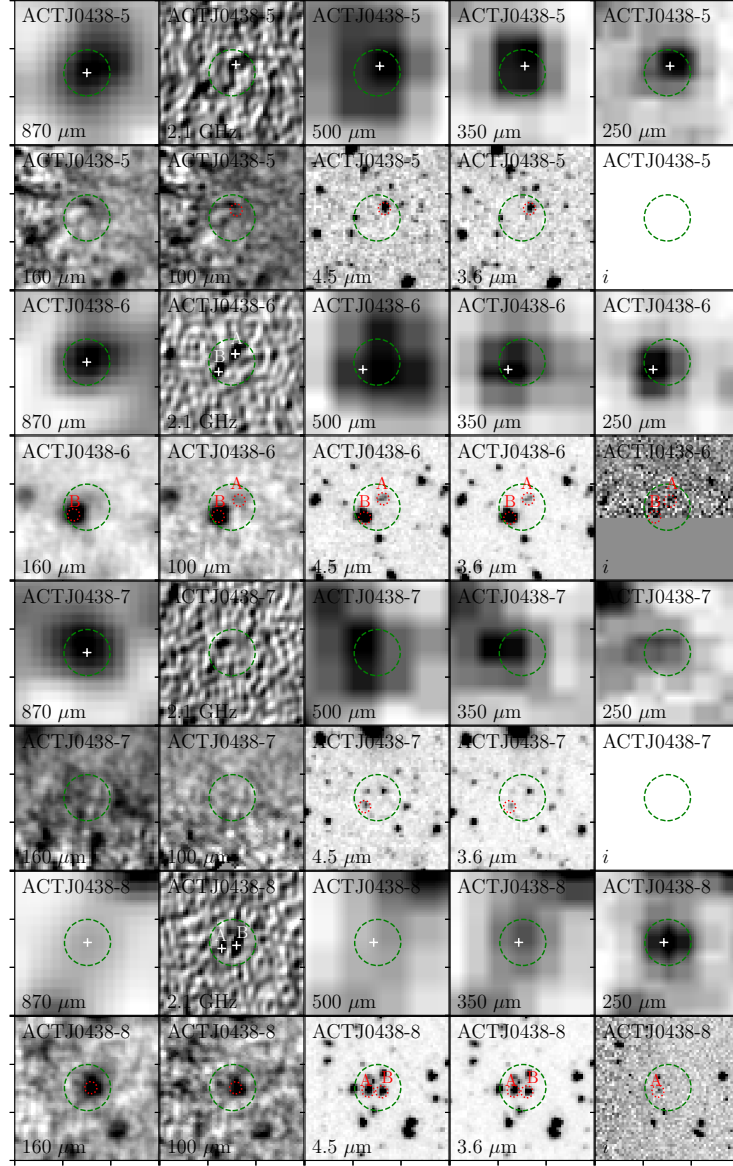


Figure 14. (Continued). Counterpart identification for SMGs detected in the field of cluster ACTJ0438.

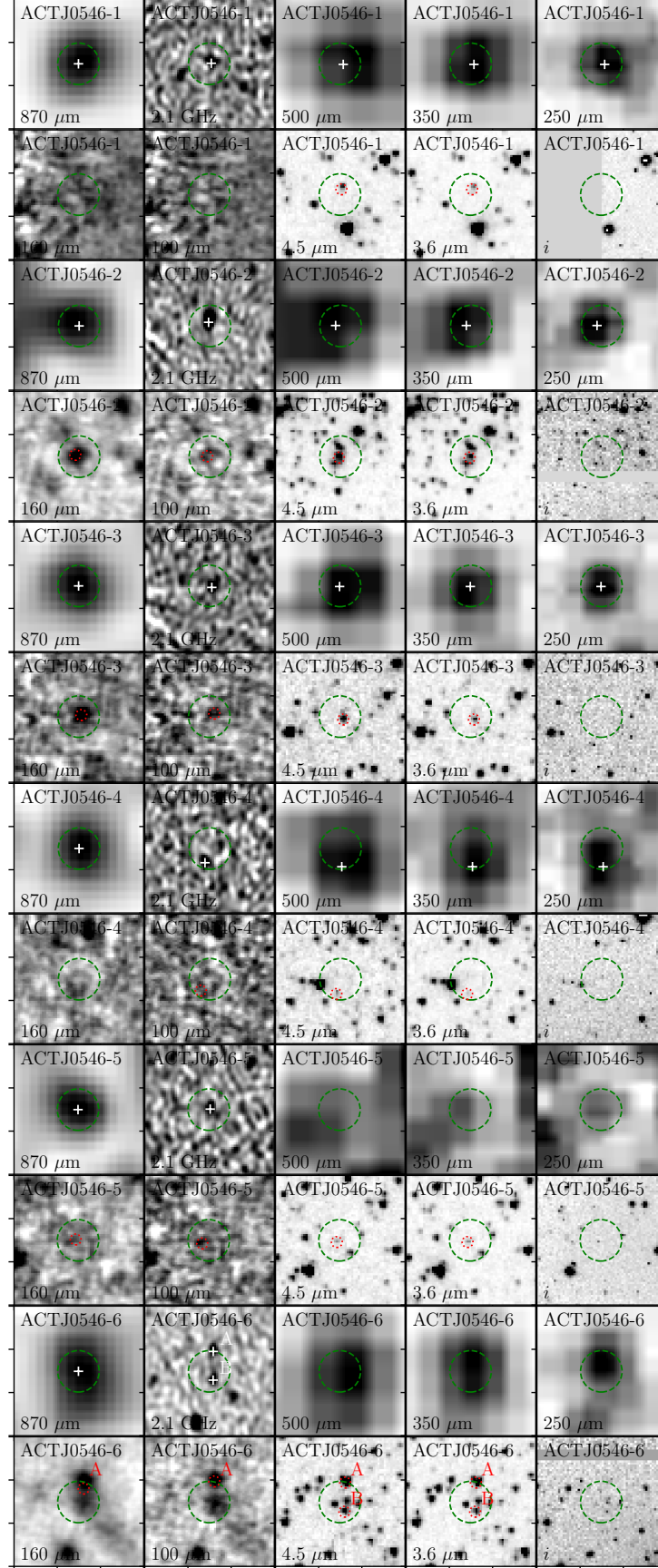


Figure 15. Counterpart identification for SMGs detected in the field of cluster ACTJ0546.

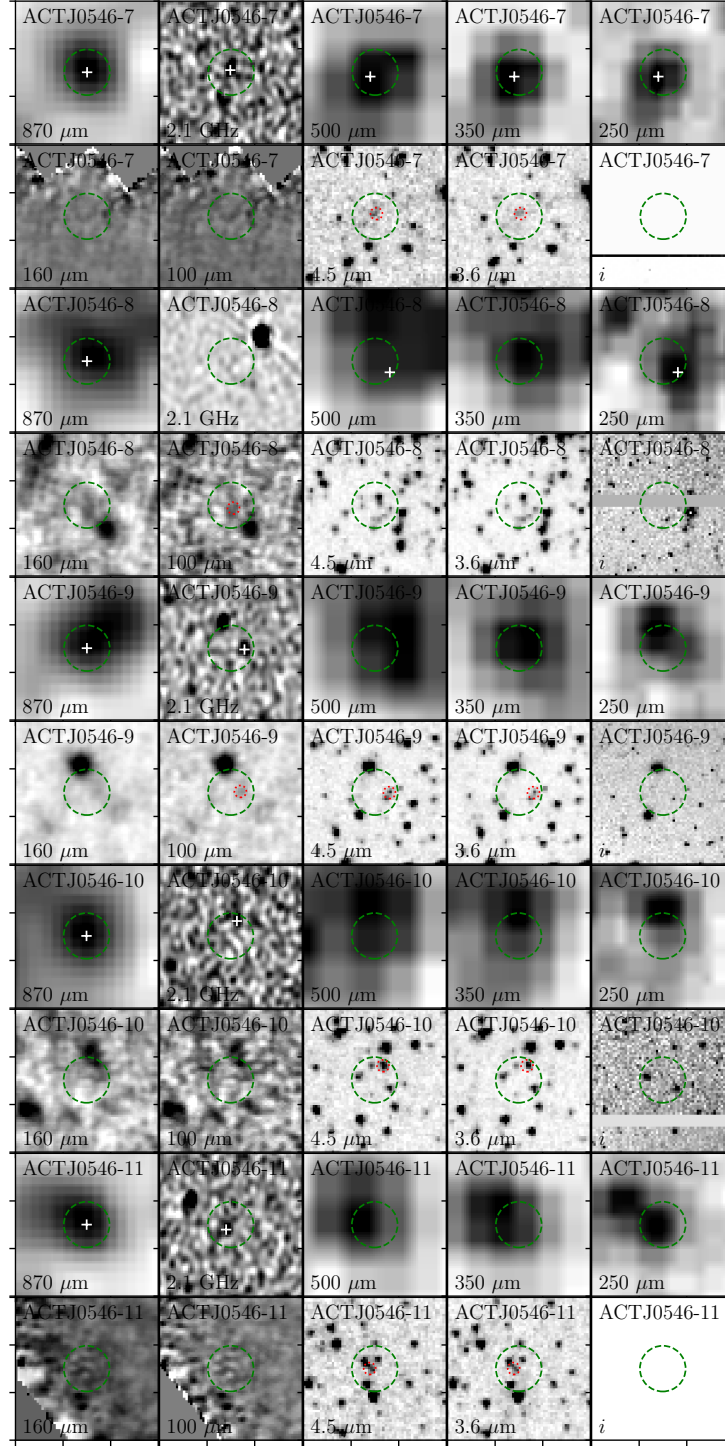


Figure 15. (Continued) Counterpart identification for SMGs detected in the field of cluster ACTJ0546.

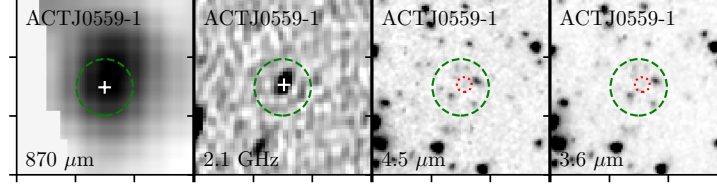


Figure 16. Counterpart identification for SMGs detected in the field of cluster ACTJ0559.

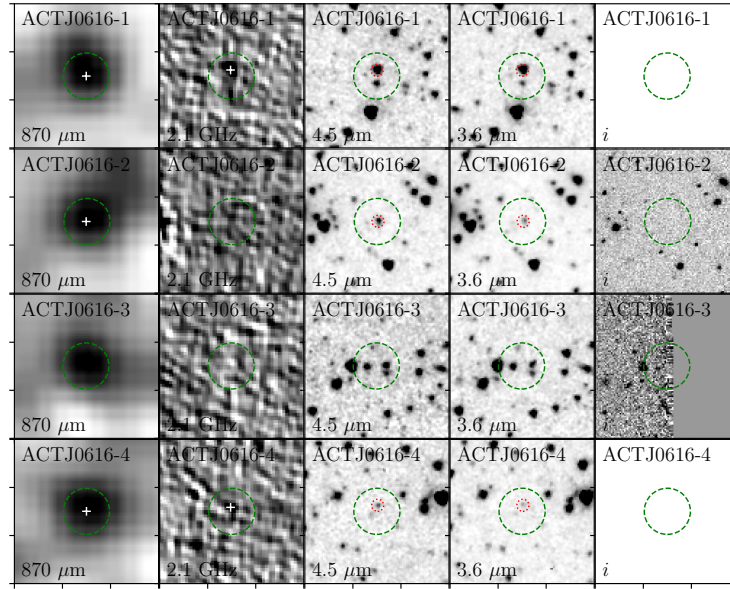


Figure 17. Counterpart identification for SMGs detected in the field of cluster ACTJ0616.

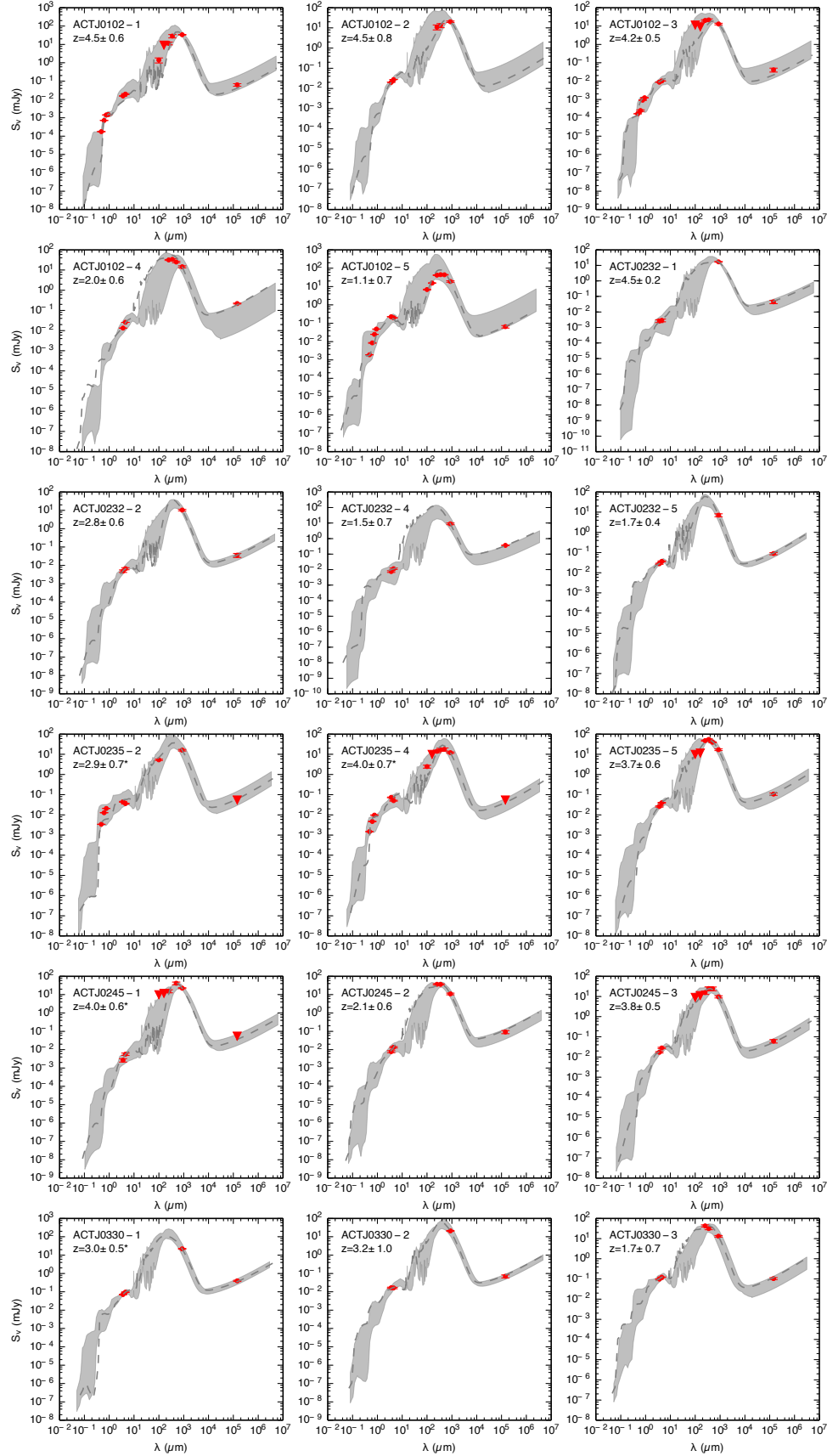


Figure 18. SED fits for LASCAR SMGs with secure or tentative counterpart identifications. For each source we plot the observed flux densities (red dots and error bars), flux density upper limits when appropriate (red downward triangles), the absolute best-fit SED, and the range of redshifted templates (shaded grey) that provide similarly good fits to the observational data (i.e., models for which the resulting χ^2 values are within 10% of their lowest values). The annotations in each panel indicated the estimated photometric redshift and error; values marked with (*) indicate tentative counterpart matches and SED fits.

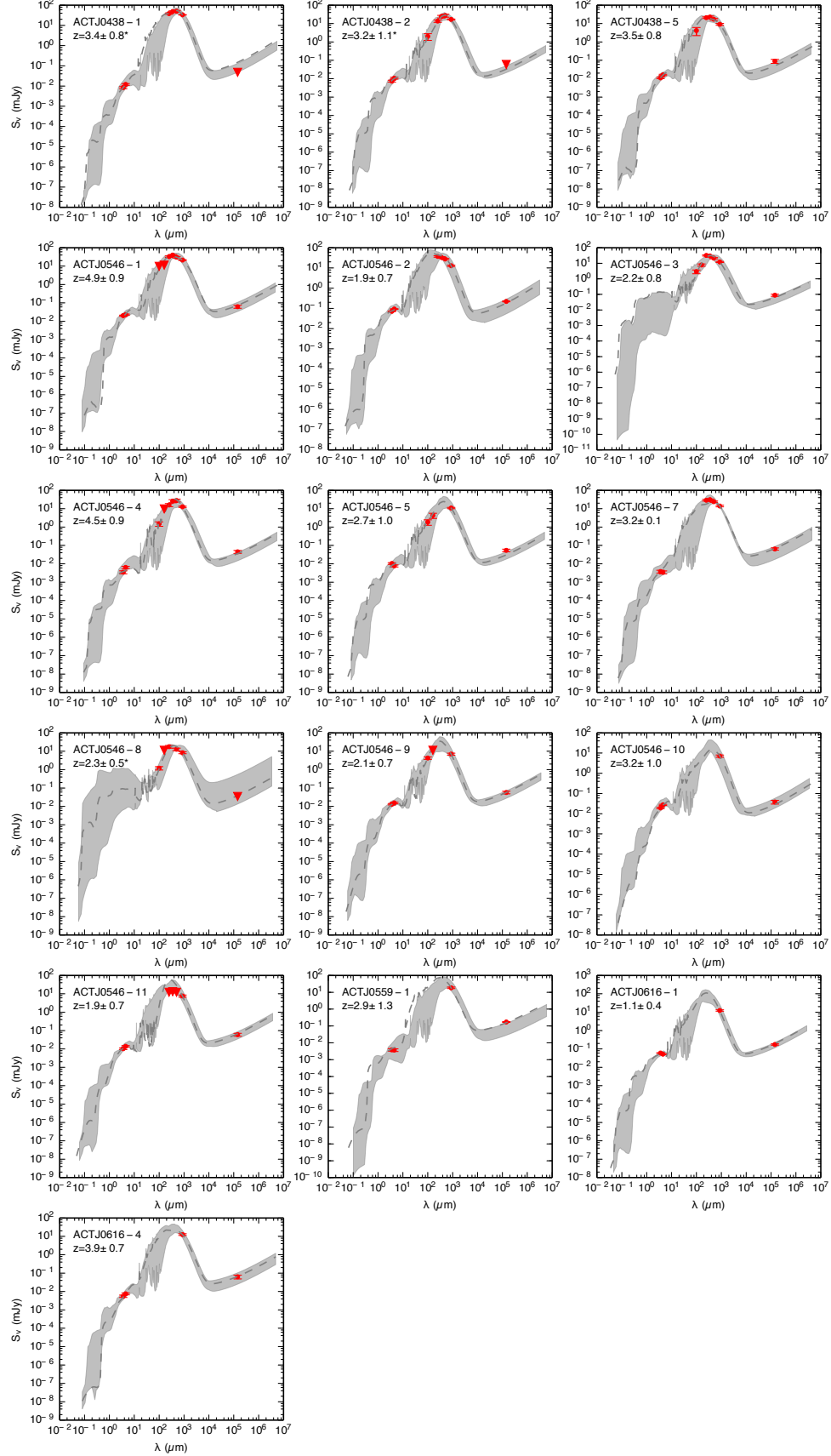


Figure 18. (Continued) SED fits for LASCAR SMGs with secure or tentative counterpart identifications.

Table 7. Radio, FIR, near-IR, and optical counterparts for SMGs detected in LASCAR clusters.

(1)	(2)	(3)	(4)	(5)	(6)	(7)	(8)	(9)	(10)	(11)	(12)	(13)	(14)	(15)	(16)	(17)	(18)	(19)
Source	$S_{2.1}$	$\Delta S_{2.1}$	S_{500}	ΔS_{500}	S_{350}	ΔS_{350}	S_{250}	ΔS_{250}	S_{160}	ΔS_{160}	S_{100}	ΔS_{100}	$S_{4.5}$	$\Delta S_{4.5}$	$S_{3.6}$	$\Delta S_{3.6}$	i_{AB}	Comment
ACTJ0102-1	63.0	10.0	28.6	6.0	11.4	2.0	1.4	0.4	19.57	0.02	15.46	0.01	25.78	S
ACTJ0102-2	13.5	3.0	13.2	3.0	11.0	3.0	27.62	0.02	20.10	0.02	...	T
ACTJ0102-3	41.0	10.0	19.1	2.0	21.7	3.0	20.2	2.0	10.2	0.02	8.72	0.01	25.85	S
ACTJ0102-4	219.0	11.0	25	2.0	34	3.0	31.7	2.0	25.7	0.02	13.30	0.01	...	S
ACTJ0102-5	65.0	10.0	43.9	2.0	44.5	2.0	42.0	2.0	15.4	0.6	6.9	0.4	198.1	0.05	225.90	0.05	23.2	S
ACTJ0215-1	N
ACTJ0215-2	38.69	0.02	30.30	0.02	...	T
ACTJ0215-3	22.1	0.02	16.76	0.01	...	T
ACTJ0232-1	45.0	11.0	2.89	0.01	2.61	0.01	...	S
ACTJ0232-2	36.0	9.0	6.63	0.01	4.87	0.01	...	S
ACTJ0232-4	366.0	11.0	11.44	0.01	7.52	0.01	...	S
ACTJ0232-5	89.0	11.0	36.75	0.02	27.77	0.02	...	S
ACTJ0235-1	135.0	21.0	43.2	2.0	61.5	3.0	68.7	3.0	2.3	0.1	36.44	0.02	26.18	0.02	...	T
ACTJ0235-2	5.3	0.4	36.17	0.02	44.63	0.02	22.57	T
ACTJ0235-3	49.0	12.0	46.1	1.0	126.8	3.0	95.8	1.7	24.1	0.7	262.3	0.06	403.60	0.07	15.83	F
ACTJ0235-4	17.7	3.0	16.9	3.0	14.1	2.0	2.5	0.4	50.63	0.02	73.65	0.03	23.47	T
ACTJ0235-5	107.0	14.0	39.6	2.0	54.8	3.0	47.7	3.0	39.48	0.02	26.01	0.02	...	T
ACTJ0245-1	41.8	7.0	15.5	3.0	5.67	0.01	2.67	0.01	...	T
ACTJ0245-2	92.0	18.0	36.3	3.0	36.7	3.0	13.44	0.01	7.76	0.01	...	S
ACTJ0245-3	61.0	12.0	24.2	5.0	24.7	5.0	15.6	3.0	28.16	0.02	17.08	0.01	...	S
ACTJ0330-1	189.0	19.0	95.32	0.03	70.73	0.03	...	T
ACTJ0330-2	70.0	13.0	16.22	0.01	16.60	0.01	...	S
ACTJ0330-3	104.0	12.0	122	0.04	98.45	0.03	...	S
ACTJ0438-1	50.3	4.0	48.5	4.0	38.2	3.0	12.06	0.01	8.37	0.01	...	T
ACTJ0438-2	27.3	5.0	24	4.0	13.7	2.0	2	0.8	10.62	0.01	7.37	0.01	25.54	T
ACTJ0438-4A	57.0	14.0	4.3	0.8	57.02	0.03	58.24	0.03	21.89	D
ACTJ0438-4B	171.0	14.0	2.69	0.01	3.25	0.01	...	D
ACTJ0438-5	90.0	22.0	17.2	2.0	22.7	3.0	20.9	2.0	4.2	2.0	16.11	0.00	11.05	0.01	...	S
ACTJ0438-6A	119.0	16.0	11.2	0.11	10.17	0.11	25.18	D
ACTJ0438-6B	110.0	13.0	6.7	0.7	29.4	1.0	49.7	2.0	30.4	2.8	16.4	1.0	105.4	0.04	154.70	0.04	23.17	D
ACTJ0438-7	8.34	0.01	6.63	0.01	...	T
ACTJ0438-8A	49.0	12.0	16.3	2.0	21.4	3.0	22.4	3.0	8.4	2.8	4.9	1.0	61.77	2.72	69.76	2.82	22.9	D
ACTJ0438-8B	158.0	14.0	77.84	0.03	74.20	0.03	...	D

Table 7 continued

Table 7 (*continued*)

(1)	(2)	(3)	(4)	(5)	(6)	(7)	(8)	(9)	(10)	(11)	(12)	(13)	(14)	(15)	(16)	(17)	(18)	(19)
Source	$S_{2.1}$	$\Delta S_{2.1}$	S_{500}	ΔS_{500}	S_{350}	ΔS_{350}	S_{250}	ΔS_{250}	S_{160}	ΔS_{160}	S_{100}	ΔS_{100}	$S_{4.5}$	$\Delta S_{4.5}$	$S_{3.6}$	$\Delta S_{3.6}$	i_{AB}	Comment
ACTJ0546-1	62.0	11.0	30.8	3.0	40.1	3.0	32.7	3.0	23.1	0.02	20.10	0.02	...	S
ACTJ0546-2	231.0	10.0	27.7	2.0	33.8	3.0	37.3	3.0	8.4	0.9	2.7	0.5	93.15	0.03	71.85	0.03	...	S
ACTJ0546-3	89.0	13.0	21.4	2.0	29.7	2.0	32.1	3.0	7.8	1.3	2.9	0.9	22.43	0.02	14.82	0.01	...	S
ACTJ0546-4	45.0	8.0	28.0	5.0	25.9	5.0	15.9	3.0	1.5	0.4	6.39	0.01	3.51	0.01	...	S
ACTJ0546-5	54.0	9.0	4.3	1.3	1.9	0.6	7.73	0.01	10.43	0.01	...	S
ACTJ0546-6A	91.0	10.0	22.3	1.0	6	0.4	84.64	3.18	68.61	2.79	...	D
ACTJ0546-6B	81.0	9.0	37.26	0.02	32.93	0.02	...	D
ACTJ0546-7	64.0	9.0	24	2.0	31.1	3.0	28.9	3.0	3.43	0.01	3.82	0.01	...	S
ACTJ0546-8	12.8	2.0	17.7	3.0	1.2	0.3	T
ACTJ0546-9	57.0	9.0	4.3	0.7	15.47	0.01	13.12	0.01	...	S
ACTJ0546-10	38.0	8.0	27.57	0.02	19.27	0.01	...	S
ACTJ0546-11	60.0	11.0	13.85	0.01	10.26	0.01	...	S
ACTJ0559-1	172.0	10.0	3.71	0.01	3.84	0.01	...	S
ACTJ0616-1	175.0	14.0	51.9	0.02	59.81	0.03	...	S
ACTJ0616-2	21.03	0.21	14.41	0.14	...	T
ACTJ0616-4	63.0	15.0	7.5	0.01	5.53	0.01	...	S

NOTE—Columns

(1) Source name. (2),(3) 2.1 GHz flux density and flux density uncertainty in μJy . (4) to (9) SPIRE 500, 350 and 250 μm flux densities and uncertainties in mJy. (10) to (13) PACS 160, 100 μm flux densities and uncertainties in mJy. (14) to (17) IRAC 4.5 μm , 3.6 μm flux densities and uncertainties in mJy. (18) i_{AB} magnitude of the optical counterpart. (19) Comment on counterpart identification: “S” indicates a secure counterpart, “D” a double counterpart identification, “T” a tentative identification, and “F” a foreground source. For radio to near-IR bands, S_λ indicates the flux density and ΔS_λ is the associated uncertainty, with λ the observing frequency in GHz (for radio measurements) or wavelength in microns (for all other measurements).

Table 8. Positions of radio, SPIRE, PACS, IRAC, and optical counterparts for SMGs detected in LASCAR clusters.

Source	2.1 GHz		SPIRE		PACS		IRAC		Optical	
	R.A.	Dec.	R.A.	Dec.	R.A.	Dec.	R.A.	Dec.	R.A.	Dec.
ACTJ0102-1	01:02:55.6	-49:15:9.4	01:02:55.6	-49:15:10.3	01:02:55.7	-49:15:08.8	01:02:55.7	-49:15:8.6	01:02:55.7	-49:15:8.0
ACTJ0102-2	01:03:14.4	-49:13:32.7	01:03:14.1	-49:13:33.4
ACTJ0102-3	01:03:5.4	-49:17:11.6	01:03:5.5	-49:17:15.3	01:03:5.4	-49:17:11.6	01:03:5.4	-49:17:11.5
ACTJ0102-4	01:03:8.3	-49:11:47.8	01:03:8.4	-49:11:47.8	01:03:8.2	-49:11:48.0
ACTJ0102-5	01:02:49.3	-49:15:5.5	01:02:49.5	-49:15:6.5	01:02:49.2	-49:15:6.2	01:02:49.4	-49:15:6.1	01:02:49.3	-49:15:6.4
ACTJ0215-2	02:15:19.2	-52:17:9.9
ACTJ0215-3	02:15:11.1	-52:11:18.4
ACTJ0232-1	02:32:50.0	-52:56:15.9	02:32:50.0	-52:56:14.9
ACTJ0232-2	02:32:57.5	-52:56:34.4	02:32:57.5	-52:56:35.0
ACTJ0232-4	02:33:0.1	-53:02:31.5	02:32:60.0	-53:02:31.9
ACTJ0232-5	02:33:9.7	-52:57:34.0	02:33:9.8	-52:57:33.8
ACTJ0235-1	02:35:38.8	-51:19:3.1	02:35:38.9	-51:19:7.9	02:35:39.0	-51:19:06.3	02:35:38.9	-51:19:4.1
ACTJ0235-2	02:35:42.5	-51:21:17.9	02:35:42.9	-51:21:16.6	02:35:42.9	-51:21:16.8
ACTJ0235-4	02:35:43.8	-51:22:44.5	02:35:42.7	-51:22:40.0	02:35:42.6	-51:22:40.1	02:35:42.6	-51:22:40.1
ACTJ0235-5	02:35:27.4	-51:18:49.5	02:35:27.6	-51:18:49.5	02:35:27.3	-51:18:46.7
ACTJ0245-1	02:45:30.7	-53:04:13.8	02:45:30.6	-53:04:11.9
ACTJ0245-2	02:45:42.1	-53:02:0.6	02:45:42.2	-53:02:4.5	02:45:41.9	-53:01:59.7
ACTJ0245-3	02:45:35.6	-53:05:3.0	02:45:35.3	-53:04:57.0	02:45:35.7	-53:05:2.7
ACTJ0330-1	03:30:30.1	-52:27:23.5	03:30:30.0	-52:27:23.6
ACTJ0330-2	03:30:54.0	-52:24:33.7	03:30:53.9	-52:24:32.8
ACTJ0330-3	03:31:14.0	-52:28:35.4	03:31:14.0	-52:28:35.1
ACTJ0438-1	04:38:29.8	-54:18:32.3	04:38:30.8	-54:18:32.1
ACTJ0438-2	04:38:34.9	-54:19:40.6	04:38:35.0	-54:19:43.9	04:38:35.4	-54:19:45.5
ACTJ0438-4A	04:38:24.4	-54:17:18.8	04:38:24.5	-54:17:17.9	04:38:24.5	-54:17:16.9
ACTJ0438-4B	04:38:24.5	-54:17:36.3	04:38:25.1	-54:17:33.2	04:38:24.5	-54:17:36.9	04:38:24.4	-54:17:18.1
ACTJ0438-5	04:38:42.3	-54:21:9.8	04:38:42.4	-54:21:10.4	04:38:42.2	-54:21:9.4
ACTJ0438-6A	04:38:24.5	-54:21:17.6	04:38:25.3	-54:21:24.1	04:38:24.3	-54:21:18.2	04:38:24.4	-54:21:17.6	04:38:24.5	-54:21:18.5
ACTJ0438-6B	04:38:25.3	-54:21:25.1	04:38:25.3	-54:21:24.1	04:38:25.3 -54:21:24.2	04:38:25.3	-54:21:25.6	04:38:25.3	-54:21:25.1	
ACTJ0438-7	04:38:19.5	-54:23:10.9
ACTJ0438-8A	04:38:33.6	-54:19:10.5	04:38:33.3	-54:19:7.9	04:38:32.9	-54:19:8.0	04:38:33.6	-54:19:09.4	04:38:33.6	-54:19:9.5
ACTJ0438-8B	04:38:32.9	-54:19:09.2	04:38:33.3	-54:19:7.9	04:38:32.9	-54:19:8.0	04:38:32.9	-54:19:9.7	04:38:33.4	-54:19:6.2
ACTJ0546-1	05:47:1.3	-53:45:24.2	05:47:1.3	-53:45:24.7	05:47:1.4	-53:45:22.1
ACTJ0546-2	05:46:34.5	-53:45:50.2	05:46:34.7	-53:45:51.7	05:46:34.7	-53:45:51.1	05:46:34.5	-53:45:52.4
ACTJ0546-3	05:46:53.9	-53:44:12.9	05:46:54.0	-53:44:12.5	05:46:53.8	-53:44:11.5	05:46:53.8	-53:44:13.6
ACTJ0546-4	05:46:37.9	-53:43:14.4	05:46:37.5	-53:43:16.3	05:46:37.8	-53:43:14.7
ACTJ0546-5	05:46:55.0	-53:46:48.4	05:46:55.2	-53:46:48.3	05:46:55.2	-53:46:49.5
ACTJ0546-6A	05:46:49.7	-53:46:13.7	05:46:49.7	-53:46:13.4	05:46:49.7	-53:46:13.9
ACTJ0546-6B	05:46:49.7 -	53:46:27.0	05:46:49.7	-53:46:27.4
ACTJ0546-7	05:46:30.1	-53:41:39.7	05:46:30.3	-53:41:42.4	05:46:30.0	-53:41:39.4
ACTJ0546-8	05:46:39.2	-53:46:7.6
ACTJ0546-9	05:46:53.1	-53:47:47.0	05:46:53.1	-53:47:46.6
ACTJ0546-10	05:46:28.1	-53:45:38.1	05:46:28.0	-53:45:38.4
ACTJ0546-11	05:47:6.2	-53:47:57.5	05:47:6.2	-53:47:55.4
ACTJ0559-1	06:00:18.4	-52:49:56.9	06:00:18.3	-52:49:56.8
ACTJ0616-1	06:16:14.0	-52:27:21.0	06:16:13.9	-52:27:21.1
ACTJ0616-2	06:16:30.2	-52:27:10.5
ACTJ0616-4	06:16:39.4	-52:22:39.3	06:16:39.3	-52:22:38.4

REFERENCES

- Abell, G. O., Corwin, Jr., H. G., & Olowin, R. P. 1989, *ApJS*, 70, 1
- Barger, A. J., Cowie, L. L., & Sanders, D. B. 1999, *ApJL*, 518, L5
- Baugh, C. M., Lacey, C. G., Frenk, C. S., et al. 2005, *MNRAS*, 356, 1191
- Berta, S., Magnelli, B., Lutz, D., et al. 2010, *A&A*, 518, L30
- Blain, A. W., Smail, I., Ivison, R. J., Kneib, J.-P., & Frayer, D. T. 2002, *PhR*, 369, 111
- Bleem, L. E., Stalder, B., de Haan, T., et al. 2015, *ApJS*, 216, 27
- Bolzonella, M., Miralles, J.-M., & Pelló, R. 2000, *A&A*, 363, 476
- Bondi, M., Ciliegi, P., Schinnerer, E., et al. 2008, *Å*, 681, 1129
- Brisbin, D., Miettinen, O., Aravena, M., et al. 2017, *ApJ*, 608, 15
- Bruzual, G., & Charlot, S. 2003, *MNRAS*, 344, 1000
- Capak, P., Carilli, C. L., Lee, N., et al. 2008, *ApJL*, 681, L53
- Carilli, C. L., & Walter, F. 2013, *ARA&A*, 51, 105
- Carlstrom, J. E., Ade, P. A. R., Aird, K. A., et al. 2011, *PASP*, 123, 568
- Casey, C. M., Narayanan, D., & Cooray, A. 2014, *PhR*, 541, 45
- Chapman, S. C., Blain, A. W., Smail, I., & Ivison, R. J. 2005, *ApJ*, 622, 772
- Chapman, S. C., Scott, D., Borys, C., & Fahlman, G. G. 2002, *MNRAS*, 330, 92
- Chen, C.-C., Cowie, L. L., Barger, A. J., et al. 2013, *ApJ*, 776, 131
- Condon, J. J. 1992, *ARA&A*, 30, 575
- Coppin, K., Chapin, E. L., Mortier, A. M. J., et al. 2006, *MNRAS*, 372, 1621
- Cowie, L. L., Barger, A. J., & Kneib, J.-P. 2002, *AJ*, 123, 2197
- Danielson, A. L. R., Swinbank, A. M., & Smail, I. 2017, *ApJ*, 840, 78
- Dannerbauer, H., Daddi, E., Morrison, G. E., et al. 2010, *ApJL*, 720, L144
- Downes, A. J. B., Peacock, J. A., Savage, A., & Carrie, D. R. 1986, *MNRAS*, 218, 31
- Edge, A. C., Boehringer, H., Guzzo, L., et al. 1994, *A&A*, 289, L34
- Egami, E., Rex, M., Rawle, T. D., et al. 2010, *A&A*, 518, L12
- Fazio, G. G., Hora, J. L., Allen, L. E., et al. 2004, *ApJS*, 154, 10
- Geach, J. E., Dunlop, J. S., Halpern, M., et al. 2017, *MNRAS*, 465, 1789
- Gehrels, N. 1986, *ApJ*, 303, 336
- Griffin, M. J., Abergel, A., Abreu, A., et al. 2010, *A&A*, 518, L3
- Güsten, R., Nyman, L. Å., Schilke, P., et al. 2006, *A&A*, 454, L13
- Hainline, L. J., Blain, A. W., Smail, I., et al. 2009, *ApJ*, 699, 1610
- Hasselfield, M., Hilton, M., Marriage, T. A., et al. 2013, *JCAP*, 7, 008
- Hauser, M. G., & Dwek, E. 2001, *ARA&A*, 39, 249
- Hilton, M., Hasselfield, M., Sifón, C., et al. 2013, *MNRAS*, 435, 3469
- Hodge, J. A., Karim, A., Smail, I., et al. 2013, *ApJ*, 768, 91
- Holland, W. S., Robson, E. I., Gear, W. K., et al. 1999, *MNRAS*, 303, 659
- Holland, W. S., Bintley, D., Chapin, E. L., et al. 2013, *MNRAS*, 430, 2513
- Hsu, L.-Y., Cowie, L. L., Chen, C.-C., Barger, A. J., & Wang, W.-H. 2016, *ApJ*, 829, 25
- Hughes, D. H., Serjeant, S., Dunlop, J., et al. 1998, *Nature*, 394, 241
- Ibar, E., Ivison, R. J., Best, P. N., et al. 2010, *MNRAS*, 401, L53
- Iglesias-Páramo, J., Buat, V., Hernández-Fernández, J., et al. 2007, *ApJ*, 670, 279
- Ivison, R. J., Smail, I., Barger, A. J., et al. 2000, *MNRAS*, 315, 209
- Ivison, R. J., Smail, I., Le Borgne, J.-F., et al. 1998, *MNRAS*, 298, 583
- Ivison, R. J., Greve, T. R., Smail, I., et al. 2002, *MNRAS*, 337, 1
- Johansson, D., Sigurdarson, H., & Horellou, C. 2011, *A&A*, 527, A117+
- Johansson, D., Horellou, C., Sommer, M. W., et al. 2010, *A&A*, 514, A77+
- Jones, D. H., Read, M. A., Saunders, W., et al. 2009, *MNRAS*, 399, 683
- Jullo, E., Kneib, J.-P., Limousin, M., et al. 2007, *New Journal of Physics*, 9, 447
- Karim, A., Swinbank, A. M., Hodge, J. A., et al. 2013, *MNRAS*, 432, 2
- Knudsen, K. K., van der Werf, P. P., & Kneib, J.-P. 2008, *MNRAS*, 384, 1611
- Komatsu, E., Smith, K. M., Dunkley, J., et al. 2011, *ApJS*, 192, 18
- Lima, M., Jain, B., & Devlin, M. 2010a, *MNRAS*, 406, 2352

- Lima, M., Jain, B., Devlin, M., & Aguirre, J. 2010b, *ApJL*, 717, L31
- Limousin, M., Richard, J., Jullo, E., et al. 2007, *ApJ*, 668, 643
- Lindner, R. R., Aguirre, P., Baker, A. J., et al. 2015, *ApJ*, 803, 79
- Magnelli, B., Lutz, D., Berta, S., et al. 2010, *A&A*, 518, L28
- Markevitch, M., Gonzalez, A. H., David, L., et al. 2002, *ApJL*, 567, L27
- Marriage, T. A., Baptiste Juin, J., Lin, Y.-T., et al. 2011a, *ApJ*, 731, 100
- Marriage, T. A., Acquaviva, V., Ade, P. A. R., et al. 2011b, *ApJ*, 737, 61
- Marsden, D., Gralla, M., Marriage, T. A., et al. 2014, *MNRAS*, 439, 1556
- McMullin, J. P., Waters, B., Schiebel, D., Young, W., & Golap, K. 2007, in *Astronomical Society of the Pacific Conference Series*, Vol. 376, *Astronomical Data Analysis Software and Systems XVI*, ed. R. A. Shaw, F. Hill, & D. J. Bell, 127
- Menanteau, F., Hughes, J. P., Jimenez, R., et al. 2009, *ApJ*, 698, 1221
- Menanteau, F., González, J., Juin, J.-B., et al. 2010a, *ApJ*, 723, 1523
- Menanteau, F., Hughes, J. P., Barrientos, L. F., et al. 2010b, *ApJS*, 191, 340
- Menanteau, F., Hughes, J. P., Sifón, C., et al. 2012, *ApJ*, 748, 7
- Menanteau, F., Sifón, C., Barrientos, L. F., et al. 2013, *ApJ*, 765, 67
- Michałowski, M., Hjorth, J., & Watson, D. 2010, *A&A*, 514, A67
- Michałowski, M. J., Hjorth, J., Castro Cerón, J. M., & Watson, D. 2008, *ApJ*, 672, 817
- Mocanu, L. M., Crawford, T. M., Vieira, J. D., et al. 2013, *ApJ*, 779, 61
- Navarro, J. F., Frenk, C. S., & White, S. D. M. 1997, *ApJ*, 490, 493
- Ott, S. 2010, in *Astronomical Society of the Pacific Conference Series*, Vol. 434, *Astronomical Data Analysis Software and Systems XIX*, ed. Y. Mizumoto, K.-I. Morita, & M. Ohishi, 139
- Pilbratt, G. L., Riedinger, J. R., Passvogel, T., et al. 2010, *A&A*, 518, L1
- Poglitsch, A., Waelkens, C., Geis, N., et al. 2010, *A&A*, 518, L2
- Postman, M., Coe, D., Benítez, N., et al. 2012, *ApJS*, 199, 25
- Reichardt, C. L., Stalder, B., Bleem, L. E., et al. 2013, *ApJ*, 763, 127
- Reynolds, J. 1994, A Revised Flux Scale for the AT Compact Array, ATNF Memo AT/39.3/040 (<http://www.atnf.csiro.au/observers/memos/d96783~1.pdf>)
- Ruel, J., Bazin, G., Bayliss, M., et al. 2014, *ApJ*, 792, 45
- Sanders, D. B., & Mirabel, I. F. 1996, *ARA&A*, 34, 749
- Sault, R. J., Teuben, P. J., & Wright, M. C. H. 1995, in *Astronomical Society of the Pacific Conference Series*, Vol. 77, *Astronomical Data Analysis Software and Systems IV*, ed. R. A. Shaw, H. E. Payne, & J. J. E. Hayes, 433
- Scott, S. E., Fox, M. J., Dunlop, J. S., et al. 2002, *MNRAS*, 331, 817
- Sehgal, N., Trac, H., Hufferberger, K., & Bode, P. 2007, *ApJ*, 664, 149
- Sehgal, N., Trac, H., Acquaviva, V., et al. 2011, *ApJ*, 732, 44
- Serjeant, S., Dunlop, J. S., Mann, R. G., et al. 2003, *MNRAS*, 344, 887
- Sifón, C., Menanteau, F., Hasselfield, M., et al. 2013, *ApJ*, 772, 25
- Sifón, C., Battaglia, N., Hasselfield, M., et al. 2016, *MNRAS*, 461, 248
- Silva, L., Granato, G. L., Bressan, A., & Danese, L. 1998, *ApJ*, 509, 103
- Simpson, J. M., Smail, I., Swinbank, A. M., et al. 2015a, *ApJ*, 799, 81
- . 2015b, *ApJ*, 807, 128
- Siringo, G., Kreysa, E., Kovács, A., et al. 2009, *A&A*, 497, 945
- Smail, I., Ivison, R. J., & Blain, A. W. 1997a, *ApJL*, 490, L5
- . 1997b, *ApJL*, 490, L5+
- Smail, I., Ivison, R. J., Owen, F. N., Blain, A. W., & Kneib, J.-P. 2000, *ApJ*, 528, 612
- Smolčić, V., Aravena, M., Navarrete, F., et al. 2012, *A&A*, 548, A4
- Smolčić, V., Karim, A., Miettinen, O., et al. 2015, *A&A*, 576, A127
- Strandet, M. L., Weiss, A., Vieira, J. D., et al. 2016, *ApJ*, 822, 80
- Su, T., Marriage, T. A., Asboth, V., et al. 2017, *MNRAS*, 464, 968
- Sunyaev, R. A., & Zel'dovich, Y. B. 1972, *Comments on Astrophysics and Space Physics*, 4, 173
- Swetz, D. S., Ade, P. A. R., Amiri, M., et al. 2011, *ApJS*, 194, 41
- Vieira, J. D., Crawford, T. M., Switzer, E. R., et al. 2010, *ApJ*, 719, 763
- Voges, W., Aschenbach, B., Boller, T., et al. 1999, *A&A*, 349, 389

- Wardlow, J. L., Smail, I., Coppin, K. E. K., et al. 2011, MNRAS, 415, 1479
- Webb, T. M., Eales, S., Foucaud, S., et al. 2003, ApJ, 582, 6
- Wei, A., Kovács, A., Coppin, K., et al. 2009, ApJ, 707, 1201
- Wei, A., De Breuck, C., Marrone, D. P., et al. 2013, ApJ, 767, 88
- Werner, M. W., Roellig, T. L., Low, F. J., et al. 2004, ApJS, 154, 1
- Wu, X.-P., & Fang, L.-Z. 1997, ApJ, 483, 62
- Zitrin, A., Menanteau, F., Hughes, J. P., et al. 2013, ApJL, 770, L15
- Zitrin, A., Fabris, A., Merten, J., et al. 2015, ApJ, 801, 44